Microprism-based two-photon imaging of the mouse inferior colliculus reveals novel organizational principles of the auditory midbrain.

Baher A. Ibrahim[1,2], Yoshitaka Shinagawa[1, 2], Austin Douglas[4], Gang Xiao[1,2,3], Alexander R. Asilador[2,3,4], & Daniel A. Llano[1,2,3,4,5]

1- Department of Molecular & Integrative Physiology, University of Illinois at Urbana-Champaign, IL, USA.

2- Beckman Institute for Advanced Science & Technology, University of Illinois at Urbana-Champaign, IL, USA.

3- Neuroscience Program, University of Illinois at Urbana-Champaign, IL, USA.

4- School of Molecular & Cell Biology, University of Illinois at Urbana-Champaign, IL, USA.

5- Carle Illinois College of Medicine, University of Illinois at Urbana-Champaign, United States, IL, USA.

Abstract:

To navigate real-world listening conditions, the auditory system relies on the integration of multiple sources of information. However, to avoid inappropriate cross-talk between inputs, highly connected neural systems need to strike a balance between integration and segregation. Here, we develop a novel approach to examine how repeated neurochemical modules in the mouse inferior colliculus lateral cortex (LC) allow controlled integration of its multimodal inputs. The LC had been impossible to study via imaging because it is buried in a sulcus. Therefore we coupled two-photon microscopy with the use of a microprism to reveal the first-ever sagittal views of the LC to examine neuronal responses with respect to its neurochemical motifs under anesthetized and awake conditions. This approach revealed marked differences in the acoustic response properties of LC and neighboring nonlemniscal portions of the inferior colliculus. In addition, we observed that the module and matrix cellular motifs of the LC displayed distinct somatosensory and auditory responses. Specifically, neurons in modules demonstrated primarily offset responses to acoustic stimuli with enhancement in responses to bimodal stimuli, whereas matrix neurons showed onset response to acoustic stimuli and suppressed responses to bimodal stimulation. Thus, this new approach revealed that the repeated structural motifs of the LC permit functional integration of multimodal inputs while retaining distinct response properties.

Introduction:

Real-world listening occurs in environments cluttered by noise. To navigate these conditions, the auditory system relies on the integration of multiple sources of input. Broad integration of neural inputs, however, comes at a potential cost. Dense convergence can lead to inappropriate cross-talk between input streams, generating a processing “soup” whereby individual neural pathways cannot be independently modulated. Therefore, highly connected neural systems need to preserve specificity of inputs in the face of massive integration (Fair et al., 2007; Sporns, Tononi, & Edelman, 2000; Tononi, Sporns, & Edelman, 1994)

Several brain systems have solved the integration/segregation problem by creating repeated structural motifs that allow independent modulation of different pathways. For example, in the basal ganglia, neurochemical periodicity of the striosome and matrix regions permits retention of functional independence of input streams in the face of massive convergence. As a result, basal ganglia direct and indirect pathways may be independently modulated, while allowing controlled crosstalk between channels (Alexander, Crutcher, & DeLong, 1990; Brimblecombe & Cragg, 2017; Draganski et al., 2008; Gerfen, 1985)

In the auditory system, the integration/segregation challenge is particularly formidable in the inferior colliculus (IC). The IC serves as a specialized integration hub because of its heavy innervation by higher auditory centers as well as by nonauditory regions. Thus, the IC stands at the crossroads between multiple brain regions and is thus important for linking acoustic stimuli with non-acoustic inputs. The IC comprises a lemniscal division, the central nucleus (ICC), that receives primarily ascending auditory projections (Oliver, 2005; Willard & Ryugo, 1983; Willott, 2001) and two non-lemniscal divisions known as the dorsal (DC) and lateral (LC) cortices that receive massive descending auditory as well as non-auditory input (Bajo & Moore, 2005; Coleman & Clerici, 1987; Loftus, Malmierca, Bishop, & Oliver, 2008; Saldaña, Feliciano, & Mugnaini, 1996; Schreiner & Winer, 2005; Winer, Larue, Diehl, & Hefti, 1998) as reviewed in (A.

M. H. Lesicko & Geffen, 2022). The LC and DC appear to differ in their strategy for integrating these inputs. The DC does not contain known structural heterogeneities but has a tonotopic arrangement of neuronal responses on its surface (Barnstedt, Keating, Weissenberger, King, & Dahmen, 2015; A. B. Wong & Borst, 2019). In contrast, the LC contains repeated neurochemical motifs, here referred to as modules, that express the inhibitory neurotransmitter GABA as well as other metabolic markers (Chernock, Larue, & Winer, 2004). Areas outside the modules, referred to as matrix, stain strongly for calretinin (Dillingham, Gay, Behrooz, & Gabriele, 2017). We and others have determined that nearly all of the long- and short-range connectivity of the LC is governed by the module/matrix organization (Dillingham et al., 2017; Lamb-Echegaray, Noftz, Stinson, & Gabriele, 2019; A. M. H. Lesicko, Sons, & Llano, 2020; A. M. Lesicko, Hristova, Maigler, & Llano, 2016). Unfortunately, how the LC integrates these inputs while maintaining distinct paths of information flow is not known. For example, LC neurons respond to multisensory stimuli (Jain & Shore, 2006; Zhou & Shore, 2006), but information from different modalities enters the LC in segregated channels (A. M. Lesicko et al., 2016). Thus, integration across the module/matrix border must occur, but the mechanisms of this integration are unknown. Traditional methods of studying the LC, such as in vivo electrophysiology, pose significant challenges in unambiguously assigning individual recorded neurons to residence in matrix or modules. Imaging approaches, such as two-photon (2P) microscopy, have proven to be enormously valuable in understanding the fine spatial structure of neural response properties in the auditory system (Bandyopadhyay, Shamma, & Kanold, 2010; Romero et al., 2020; Rothschild, Nelken, & Mizrahi, 2010). However, because of its superficial location on the dorsal surface of the mouse midbrain, the DC is the only part of the IC that has been characterized by 2P imaging (Barnstedt et al., 2015; Ito, Hirose, Murase, & Ikeda, 2014; A. B. Wong & Borst, 2019). Optically, it has been impossible to characterize the functions of the LC, which is laterally embedded deep in a brain sulcus. Here, we describe a novel approach using a 45° microprism inserted into the sulcus that separates the LC from the cerebellum to investigate the fine-scale

99 functional organization of the LC from its lateral surface through 2P imaging. The 2P images
100 obtained from the microprism revealed the first-ever images of the LC in vivo showing its
101 characteristic GABAergic modules. Compared to the DC imaged from the surface, the
102 acoustically and somatosensory-evoked calcium signals obtained by the 2P imaging of the LC
103 through the microprism revealed functional distinctions between the different cellular motifs of
104 the LC. For instance, while modules were more responsive to somatosensory stimulation than
105 matrix, the latter was more acoustically-responsive and had a lower detection threshold for
106 complex sounds. Additionally, modules and matrix were found to differently process the spectral
107 and temporal features of the acoustic information. These findings suggest that the non-
108 lemniscal divisions of the IC contain rich but distinct platforms for the processing of different
109 features of auditory and non-auditory information.

110 **Results:**

111 **The insertion of 45° microprism for imaging the LC from the side.**

112 GAD67-GFP knock-in mice on a Swiss Webster background were crossed with Thy1-
113 jRGECO1a mice to produce a GAD67-GFPx jRGECO1a hybrid mouse, which was used to
114 visualize GABAergic modules, to identify the dense network of GABAergic neurons and
115 terminals in modules of the LC in the green channel (Tamamaki et al., 2003), and the calcium
116 indicator, jRGECO1a, in the red channel (Dana et al., 2018). A standard craniotomy was
117 performed (Goldey et al., 2014) with modifications to suit the specific characteristics of the IC in
118 terms of its location, depth, and high density of the surrounding vasculature (Xiong et al., 2017).
119 The craniotomy (~ 3 x 4 mm) did not drill directly into the sagittal and lambdoid sutures which
120 allowed minimal disruption of the superficial sinuses below the skull (Figure 1A) as indicated by
121 the minimal bleeding near the bone flap (Figure 1B). During drilling, pressurized air and a cold
122 stream of saline were used to remove the bone debris and dissipate heat. Because the IC sits
123 deeper in the brain compared to the surrounding structures, the direct insertion of the 45°

124 microprism was found to push the IC ventrally. Therefore, a fine diamond knife was used to
125 separate the lateral surface of the IC from the surrounding tissues without damaging the
126 transverse and sigmoid sinuses (Figures 1C and D). This step was followed by a gentle
127 retraction of the knife medially to generate a pocket to secure the microprism (Figure 1E). The
128 successful insertion of the microprism was assessed by examining the reflection of the diamond
129 knife from the microprism's top glass surface (Figures 1F and G). Holding the microprism down
130 and retracting the knife upward simultaneously resulted in securing the microprism in its pocket
131 (Figure 1H and I). Locking the microprism down in its pocket for 10 minutes with the diamond
132 knife (Figure 1J) is critical to ensure that the microprism is stabilized and to prevent bleeding.
133 Filling the gap between the skull surface and the microprism with saline was found to generate
134 motion artifact due to the heart pulsation, so 1% agarose was used to fill the gap to reduce the
135 motion artifact and add more stability to the microprism (Figure 1K). To compare response
136 properties between the LC and DC, direct imaging (i.e., without a microprism) of the dorsal
137 surface of the IC, where the DC is located, was also conducted by scanning the DC surface
138 from the most medial to lateral regions following the convex curvature of the surface (Figures 1L
139 and M).

140 **The 2P characterization of GABAergic and non-GABAergic neuronal distribution on the**
141 **LC and DC surfaces with histological validation.**

142 Following the surgery, the anesthetized animals were taken immediately for imaging.
143 Examination of the distribution of GABAergic modules in the LC was critical to validate the
144 target area for functional calcium imaging. Therefore, the 920 nm laser beam was initially used
145 to scan for GFP, which is expressed in the GABAergic cells of GAD67-GFP knock-in mice. The
146 insertion of the microprism was initially viewed by low magnification fluorescence imaging of the
147 GFP signals from the whole surface of the IC along with the inserted microprism (Figure 2A).
148 This step validated the location of the microprism relative to the IC under the microscope and

149 ensured there was no bleeding that could block the field of view. The 2P images of the GFP
150 signals from the LC imaged via the microprism across different animals revealed the LC
151 characteristic GABAergic modules (Figures 2C and E, the irregular white lines), which were
152 consistent with previous 3D reconstructions of modules from the coronal sections (Chernock et
153 al., 2004; A. M. Lesicko et al., 2016). To further validate the microprism location and the ability
154 to image the LC from the lateral surface, a laser lesion (see Methods) was created via the
155 microprism (Figure 2G), which was validated histologically (Figure 2H). For comparison, the
156 whole dorsal surface of the IC was scanned from medial to lateral borders (Figure 2B, the
157 dotted white lines). Unlike the LC, most of the dorsal surface of the IC showed a non-clustered
158 distribution of the GABAergic cells (Figures 2D and F, blue boxes). However, the lateral horizon
159 of the IC dorsal surface showed clusters of GABAergic cells and terminals that were confirmed
160 to be modules, which comprise the prominent feature of the LC (Figures 2D and F, red boxes).
161 To further validate the presence of GABAergic modules in the dorsolateral surface of the IC, a
162 laser lesion was created in a GABAergic module located in that area (Figures 2I and J, dotted
163 red circle), which was confirmed histologically (Figure 2K), demonstrating that it is possible to
164 image a portion of the LC directly from its dorsal surface.

165 Using the 1040 nm laser, the GAD67-GFPx jRGECO1a hybrid mouse showed a non-clustered
166 cellular expression of jRGECO1a on the surface of the DC (Figure 3A) or on the surface of the
167 LC imaged via microprism (Figure 3B), as expected. The IC of anesthetized animals in each
168 experimental setup was then imaged to measure calcium signals over the course of
169 pseudorandom presentations of either 500 ms pure tones of different combinations of
170 frequencies (5-40 kHz, half octave intervals) and sound levels (40-80 dB SPL, 10 dB intervals)
171 or broadband noise without or with amplitude modulation (AM-noise) of different combinations of
172 AM frequencies (2-256 Hz, one-octave intervals) and sound levels (40-80 dB SPL, 10 dB
173 intervals). As shown by two representative cells from the DC imaged from the dorsal surface or

174 LC imaged via microprism, these acoustic stimulation paradigms successfully elicited transient
175 cellular calcium signals that varied depending on the stimulus type (Figures 3C and D).

176 **Acoustic responsiveness differs in the LC and DC:**

177 As indicated by the GFP signals and consistent with Figure 2, imaging the LC of the hybrid mice
178 via microprism showed clusters of GABAergic modules, which take different irregular shapes on
179 the surface of the LC (Figure 4A - irregular white lines). Based on the best pure tone frequency
180 of each responsive cell (Barnstedt et al., 2015), an inconsistent and fragmentary tonotopic
181 organization was seen over the LC imaged via microprism (Figure 4B). For comparison, the
182 surface of the DC was imaged directly from the dorsal surface using the routine imaging setup.
183 To view the majority of the DC surface, imaging was done by scanning the DC from its medial to
184 the lateral horizon to generate a composite map (see Methods). As indicated by the GFP
185 signals, it was noted that the most lateral region of the surface of the IC showed clusters of the
186 GABAergic cells and terminals (i.e., modules, Figure 4C – irregular white lines) and are
187 therefore considered part of the LC. Based on the best pure tone frequency of each responsive
188 cell (Barnstedt et al., 2015), the DC showed a tonotopic organization of cells along the
189 rostromedial to caudolateral axis tuned to lower or higher frequencies, respectively (Figure 4D).
190 This tonotopic organization is similar to those previously described (Barnstedt et al., 2015; A. B.
191 Wong & Borst, 2019). It was also noticed that a large area of the DC was tuned to the lowest
192 tested frequency (5kHz), suggesting a low frequency bias on the surface of the DC. To quantify
193 tuning differences between DC and LC, the cumulative distribution function based on the cells'
194 best frequency showed a low-frequency bias in the DC, similar to previous work (Ito et al., 2014;
195 Romand & Ehret, 1990; Shen, Xu, & Shen, 2003; Stiebler & Ehret, 1985), while most of the LC
196 cells imaged via microprism were tuned to higher frequencies (Figure 4E, Mann-Whitney Test: z
197 $= -13.4$, $p < 0.001$, a median of best-tuned frequency = 5 and 7.5 Hz for DC and LC via
198 microprism, respectively).

Detection of AM is critical to identify natural sounds as well as to aggregate sound sources during auditory scene analysis, which is important for communication (Joris, Schreiner, & Rees, 2004; Rees & Langner, 2005; Singh & Theunissen, 2003). The IC also is the first site in the ascending auditory pathway where a substantial number of neurons are rate-tuned to AM (Frisina, 2001; Joris et al., 2004; Langner, 1992; Nelson & Carney, 2007; Rabang et al., 2012). Even though calcium indicators do not provide a spike-by-spike readout of neural activity, their integrated signal does correlate with the number of spikes produced by a neuron over short time windows (Vogelstein et al., 2010; Yaksi & Friedrich, 2006). Thus, this integrated signal can be used to measure rate responses to AM. Using this integrated signal, we tested the ability of the cells of LC imaged via microprism in its different motifs to respond to broadband noise at different AM rates. We observed a significant fraction of cells that did not respond to pure tones responded to AM-noise (Figure 5A, paired-sample t-test: $t_{(6)} = -11.13$, $p = 3.1\times10^{-5}$, the percentage of responsive cells mean ± SEM = 34.7 ± 9.2% and 56.2 ± 8.9% for pure tones and AM-noise, respectively). We also observed that modules and matrix differentially process the temporal information. For instance, the matrix had a significantly greater fraction of cells that respond only to AM-noise compared to the modules (Figure 5B – striped blue bar, Mann-Whitney Test, $p = 0.02$), which suggests that neurons in the matrix are more sensitive to complex sounds compared to those in the modules. In contrast, both cellular motifs had similar fractions of cells that are responsive to pure tones (Figure 5B – solid blue bar, Mann-Whitney Test, $p = 0.58$). These findings suggest that neurons in the matrix are more responsive to sounds of greater spectral and temporal complexity than those in the modules. In the DC, like the LC imaged via microprism, a significant fraction of cells that did not respond to pure tones did respond to AM-noise (Figure 5C, paired samples t-test: $t_{(3)} = -5.8$, $p = 0.01$, the percentage of responsive cells mean ± SEM = 78.4 ± 3.6% and 97.3 ± 0.4% for pure tones and AM-noise).

Regardless of the sound type, animals showed a lower fraction of responsive neurons to the acoustic stimulation in the LC imaged via microprism compared to DC (pure tone: two-sample t-test, $t_{(9)} = 2.9$, $p = 0.008$, the percentage of responsive cells mean ± SEM = 78.4±3.6.0% and 34.7±9.2% for DC and LC, respectively, AM-noise: two-sample t-test, $t_{(9)} = 3.5$, $p = 0.008$, the percentage of responsive cells mean ± SEM = 97.3±0.4% and 56.2±8.9% for DC and LC, respectively). To evaluate if any optical artifacts due to imaging through a prism could be responsible for this finding, the number of responsive cells imaged from the lateral-most dorsal surface of the IC, which we consider part of the LC because of the presence of GABAergic modules (LC imaged from the dorsal surface), was quantified and compared with that obtained from the LC imaged via microprism. We observed that there were no significant differences between the number of tone or noise-responsive neurons between the LC imaged via microprism or directly from the dorsal surface (pure tone: two-sample t-test, $t_{(9)} = 1.1$, $p = 0.28$, AM-noise: two-sample t-test, $t_{(9)} = 1.6$, $p = 0.14$).

LC and DC respond differently to spectral and temporal modulation of acoustic inputs:

Given that more cells from LC imaged via microprism and DC had responses to AM-noise compared to pure tones, we further quantified the selectivity to spectral or temporal modulation by computing the spectral modulation index (SMI) or the temporal modulation index (TMI), respectively, for all the responsive cells (see Methods) across the tested sound levels.

For the LC imaged via microprism, the LC matrix has a greater proportion of spectrally modulated cells than modules most prominently at sound levels below 70 dB (Figure 5D, two-way ANOVA: $p = 7.1\times10^{-7}$, 1.0, and 0.01 for the region, sound level, and interaction, respectively, the percentage of modulated cells mean ± SEM for modules vs. matrix) suggesting that the cells in the matrix have a lower threshold to detect complex spectral features of sound. Similarly, the matrix had more cells responsive to temporal modulation as a main effect (Figure

5E, two-way ANOVA, $p = 7.1 \times 10^{-7}$, 1.0, and 0.32 for the region, sound level, and interaction, respectively), which was consistent with the above results (Figure 5B).

The DC and LC imaged via microprism were found to have different profiles of modulation of responses to spectral and temporal complexity. Although there is a general trend for SMI and TMI to decrease with increasing sound-pressure level, corresponding to an increase in pure-tone responsiveness, overall there is a statistically-significant higher level of average SMI and TMI in the LC compared to the DC (Figures 5F and G, SMI: two-way ANOVA, $p < 0.001$ for all region, sound level, and interaction, TMI: two-way ANOVA, $p < 0.001$ for all regions, sound level, and interactions). These results suggested that neurons in the LC are more sensitive to spectral and temporal modulation than those in the DC.

LC modules and matrix differentially respond to acoustic and somatosensory stimuli:

Somatosensory inputs from many cortical and subcortical structures have been identified in the non-lemniscal division of the IC, particularly in the LC (A. M. Lesicko et al., 2016; Lohse, Zimmer-Harwood, Dahmen, & King, 2022; Zhou & Shore, 2006) Previous work has shown that while somatosensory projections mostly target the modules, the auditory projections tend to target the matrix (A. M. Lesicko et al., 2016), which indicates that the LC is a multisensory integration site. Therefore, we examined the somatosensory and auditory cellular responses on the surface of the LC by coupling the 2P imaging with the microprism with a whisker or acoustic stimulation (see Methods). Acoustic stimulation was done with 500 ms broadband noise at 80 dB SPL. After the acoustic or somatosensory stimulation, evoked cellular responses were observed from the LC neurons imaged via microprism either at the beginning of the stimulation (Figures 6A and B – onset responses) or at the termination of the stimulation (Figures 6C and D – offset responses).

Auditory and somatosensory responses were evoked in the neurons of both matrix and modules imaged via microprism (Figures 7A, B, and D) and the cells were categorized within each motif into cells that respond only to acoustic stimulation, only to somatosensory stimulation, or to both stimuli (Figure 7F). The quantification of the percentage of cells in both modules and matrix revealed that the percentage of responsive cells to sound only was higher than that of cells responsive to somatosensory stimulation or those responsive to both stimuli with no preference (Modules: Figure 7H, one-way ANOVA, $p = 4.0 \times 10^{-5}$, the percentage of responsive cells mean ± SEM = 41.9 ± 5.4% (auditory-only response), 4.2 ± 0.8% (somatosensory-only response), and 10.2 ± 1.4% (auditory + somatosensory responses)) (Matrix: Figure 7I, One-way ANOVA, $p = 2.4 \times 10^{-4}$, the percentage of responsive cells mean ± SEM = 43.7 ± 8.5% (auditory response), 0.88 ± 0.36% (somatosensory response) and 2.9 ± 0.34% (auditory + somatosensory responses)). However within the pool of responsive cells and normalized against modules, we observed that more sound-responsive cells were found in the matrix, while more somatosensory responsive cells were found in the modules (Figures 7B, D, F, and J, Mann-Whitney Test, p = 0.028), which was consistent with the reported difference in inputs to modules compared to matrix (A. M. Lesicko et al., 2016). Most of the acoustically-responsive cells in the matrix showed onset responses, and the cells showing acoustically-driven offset responses were clustered in the modules (Figures 7C and K, Mann-Whitney Test, p = 0.028).

Additionally, most of these auditory-offset cells were also responsive to somatosensory stimulation as shown by the merged responses (Figure 7F), which suggests a multisensory integrative function by those cells as discussed later. Given the specific spatial location of the somatosensory-responsive cells in the modules which contain clusters of GABAergic cells, we asked if somatosensory stimulation could suppress the auditory response when both stimuli are presented simultaneously (bimodal stimulation). To test this hypothesis, we calculated and visualized the response index (RI), which was calculated as the ratio of the cellular response to

295 bimodal stimulation to the cellular response to acoustic response alone for auditory-responsive
296 cells. We observed that cells in the modules had a higher odds of having an enhancement
297 response to bimodal stimulation than matrix, while cells in the matrix had a higher odds of
298 having a suppressive response to bimodal stimulation (Figures 7G and L, enhanced response:
299 Mann-Whitney Test, $p = 0.028$, matrix median odds = 0.68, suppressed response: Mann-
300 Whitney Test, $p = 0.028$, matrix median odds = 1.33). These data suggest that the
301 module/matrix system permits preservation of distinct multimodal response properties in the
302 face of massive integration of inputs in the LC.

303 Consistent with the above data, the LC imaged from the dorsal surface (Figures 8A-D,
304 dorsolateral) shared common response profiles with the LC. For instance, the LC imaged via
305 microprism or directly from the dorsal surface had a higher percentage of somatosensory
306 responsive cells than the DC (Figure 8A-D, dorsal and dorsomedial) as quantitatively shown
307 (Figure 8H, one-way ANOVA, $p = 0.02$, the percentage of somatosensory responsive cells
308 mean ± SEM = 1.3 ± 0.83% (DC), 8.2 ± 2.4% (LC imaged from the dorsal surface), and 8.1 ±
309 0.64% (LC imaged via microprism), which suggest that the LC is the main region of the IC shell
310 that processes somatosensory information, consistent with the anatomical reports (Aitkin,
311 Dickhaus, Schult, & Zimmermann, 1978; Jain & Shore, 2006; A. M. Lesicko et al., 2016; Liu et
312 al., 2023). The matrix of the LC imaged from the dorsal surface had more responsive cells to
313 sound (Figures 8E and I, Mann-Whitney Test, $p = 0.028$, the matrix:module median ratio = 1.5),
314 and less responsive cells to somatosensory stimulation compared to its modules (Figures 8E
315 and I, Mann-Whitney Test, $p = 0.028$, matrix:module median ratio = 0.28). Additionally, more
316 acoustically onset responsive cells were found in the matrix (Figures 8F and J, Mann-Whitney
317 Test, $p = 0.028$, matrix:module median ratio = 10.2), while more acoustically offset responsive
318 cells were found in the modules (Figures 8F and J, Mann-Whitney Test, $p = 0.028$,
319 matrix:module median ratio = 0.02). More acoustically responsive cells in the matrix displayed

suppressed responses following the bimodal stimulation (Figures 8G and K, Mann-Whitney Test, & p = 0.028, matrix:module median ratio = 1.5). In contrast, more acoustically responsive cells in the modules displayed enhanced responses following the bimodal stimulation (Figures 8G and K, Mann-Whitney Test, & p = 0.028, matrix:module median ratio = 0.42). These data confirmed the findings obtained from the LC imaged via microprism and emphasized the functional difference between the LC and DC.

LC and DC differ in their acoustic and multimodal response properties in awake animals:

To determine if the presence of ketamine/xylazine anesthesia influenced the response properties detailed above, additional experiments were performed in awake animals (n=6 total, 3 from LC using prism and 3 from dorsal surface). Similar to what was observed under anesthesia, the cells of the LC imaged via microprism did not show clear evidence for tonotopy (Figure 9B). In contrast, the data obtained from imaging the DC under awake preparations showed a similar tonotopic map (Figure 9D) as that observed under anesthesia, though a greater proportion of high-frequency cells were observed leading to the observation of a low-frequency border similar to the previous under awake preparations (A. B. Wong & Borst, 2019). Similar to the results obtained under anesthesia, the LC imaged via microprism had more cells tuned to higher frequencies compared to the DC (Figure 9E, Mann-Whitney test, $p=1.6x10^{-6}$, a median of best-tuned frequency = 10 and 5 kHz for LC and DC, respectively). Both LC imaged via microprism and DC imaged directly from its dorsal surface were more responsive to AM-noise than pure tones (Figure 9F, DC: χ^2 test = 15.1, p = 0.001, the percentage of responsive cells = 72.3 vs. 78.2% for pure tone vs. AM-noise, respectively, LC: χ^2 test = 43.6, $p = 1.8x10^{-9}$, the percentage of responsive cells = 58.7 vs. 76.1% for pure tone vs. AM-noise, respectively). Within each stimulus type, while the DC was found to have more responding cells to pure tone than LC imaged via microprism (Figure 9G, χ^2 test = 39.5, $p = 1.3x10^{-8}$, the percentage of responsive cells = 72.3 vs. 58.7% for DC vs. LC, respectively), both areas showed similar

percentage of responsive cells to AM-noise (Figure 9G, χ^2 test = 1.2, p = 0.75, the percentage of responsive cells = 78.2 vs. 76.1 % for DC vs. LC, respectively, respectively). Additionally, the matrix also showed more responsive cells to sound compared to the modules regardless of the stimulus type (Figure 9H, pure tone: χ^2 test = 31.9, p = 5.2×10^{-7}, the percentage of responsive cells = 30.8 vs. 69.2% for modules vs. matrix, respectively, AM-noise: χ^2 test = 11.1, p = 0.01, the percentage of responsive cells = 37.6 vs. 62.4% for modules vs. matrix, respectively).

For somatosensory responses, similar to the anesthetized preparation, neurons in modules imaged via microprism had more cells responsive to somatosensory stimulation than the matrix, while the latter had more responsive cells to broadband noise (Figures 10A, C, E, and G, auditory response: χ^2 test = 31.9, p = 5.2×10^{-7}, the percentage of responding cells = 22 vs. 78% for modules vs. matrix, respectively, somatosensory response: χ^2 test = 11.1, p = 0.01, the percentage of responding cells = 63.6 vs. 36.4% for modules vs. matrix, respectively). Similar to anesthetized data, we found that most of the auditory responsive cells in the modules and matrix had suppressed auditory responses following bimodal stimulation (Figures 10F and H, χ^2 test = 31.9, p = 5.2×10^{-7}, matrix: The percentage of responding cells = 69.6 vs. 30.4% for suppressed vs. enhanced responses, respectively, modules: The percentage of responding cells = 95 vs. 5% for suppressed vs. enhanced responses, respectively), indicating an overall suppression in the cellular auditory response.

Discussion:

Summary:

As a new imaging approach, a microprism was used to image the LC surface, to provide the first-ever sagittal image of the LC in vivo and to examine its functional organization, which revealed the distinction between strategies used by LC and DC for processing acoustic and non-acoustic information. Imaging the LC either via microprism or from the dorsal surface

revealed that it contains GABAergic modules that were embedded in mostly non-GABAergic matrix. Although modules and matrix were found to be activated by somatosensory and auditory stimuli, they were functionally distinct. The matrix had more auditory-responsive cells with a lower threshold for complex sound detection and had more cells responsive to complex spectral and temporal auditory features than modules. In contrast, modules had more somatosensory responsive cells, consistent with anatomical differences in input to the modules compared to matrix (A. M. Lesicko et al., 2016). Somatosensory stimulation suppressed auditory responses in the matrix, suggesting that multisensory interactions exist between the matrix and modules.

The novelty of the imaging setup and technical considerations

Microprism-based 2P- microscopy has been successfully used to image the cortical layers in the somatosensory and visual cortices of mice (Andermann et al., 2013) and to image other inaccessible cortical surfaces like those folded in the brain sulci such as the medial prefrontal cortex (Low, Gu, & Tank, 2014) or entorhinal cortex (Beckmann et al., 2019; Heys, Rangarajan, & Dombeck, 2014; Low et al., 2014). In those studies, the glass window glued to the microprism was used, which requires significant skill and potential removal of brain regions to allow prism access (Heys et al., 2014). Another approach is to use a micro metal or diamond-made knife to create a pocket with minimal tissue damage (Andermann et al., 2013; Marks & Goard, 2021). Accordingly, we combined and modified some of these procedures to improve the microprism implantation to image the sagittal surface of the LC, which is deeply embedded into the brain tissue in a highly vascular area, with minimum damage to the IC or the surrounding vasculature.

Previous work using microprisms has been done chronically for up to 60 days (Heys et al., 2014; Low et al., 2014; Wenzel, Hamm, Peterka, & Yuste, 2017), with minimal tissue inflammation (Andermann et al., 2013). The current study was initially done on anesthetized animals to examine and validate the new approach, which later revealed similar organizational differences between LC and DC in awake animals. Although imaging through a microprism and

1-mm cover glass appears to have minimal impact on image quality compared to direct 2P imaging (Chia & Levene, 2009), it was important to compare LC imaging via microprism with the direct 2P imaging of the dorsal surface to validate the new imaging method. We found no significant differences between LC response properties when imaging via microprism or imaging directly from the dorsal surface. However, we did observe significant functional differences between the LC and the DC.

Responsiveness to spectral and temporal features.

While the LC showed inconsistent and fragmented tonotopy, the DC showed a consistent one, as previously reported (Barnstedt et al., 2015; A. B. Wong & Borst, 2019). However, the surface of the DC was biased to lower frequencies compared to LC, consistent with previous imaging and recording studies (Ito et al., 2014; Romand & Ehret, 1990; Shen et al., 2003; Stiebler & Ehret, 1985). Despite their response to pure tones, the DC and LC, particularly in the matrix, were more responsive to AM-noise, which fits their function as nonlemniscal divisions (Chen, Cheng, Ito, & Song, 2018; Faye-Lund & Osen, 1985; Loftus et al., 2008).

The spectral and temporal features of animal vocalization and speech are not independent (Singh & Theunissen, 2003). We observed that LC neurons, particularly in the matrix, had greater responsiveness to spectral and temporal modulation than the DC. Given the role of inhibition in the spectral and temporal processing (Cai et al., 2018; Chang, Bao, Imaizumi, Schreiner, & Merzenich, 2005; Wehr & Zador, 2003), GABAergic cells of the modules could play an important role to increase the spectral and temporal modulation indices, especially at lower sound levels, which could be critical for localizing objects in noisy environments given the importance of spectral and temporal cues for sound localization (Davis, Ramachandran, & May, 2003; Goodman, Benichoux, & Brette, 2013; Sinex, 2005). Therefore, future work is critical to image the functional responses of the GABAergic cells of the modules and compare them with the non-GABAergic cells inside and outside the modules.

Somatosensory vs. auditory responses:

In the LC, we observed that most auditory-responsive neurons, particularly onset-responsive neurons, were found in the matrix, which receives mostly auditory inputs (A. M. Lesicko et al., 2016). However, a subpopulation of acoustically-driven offset-responsive neurons preferably resides in the modules compared to the matrix. Given that the offset response could be generated as a rebound to the termination of the ongoing inhibition during the sound presentation (Xu, 2014), GABAergic cells in the modules could play an important role in the coding of sound termination as found before in the cortex (Solyga & Barkat, 2021). Because some of the offset acoustically-driven cells inside the modules were also activated by the somatosensory stimulation, this fraction of cells could then encode the termination of somatosensory-associated sounds through the local inhibitory circuits of the modules. Under in-vivo recording of the mouse IC, the offset responses were previously reported from cells that were non-GABAergic and located in the caudal and shallower parts of the IC (Kasai, Ono, & Ohmori, 2012).

Consistent with previous reports (Aitkin et al., 1978; Aitkin, Kenyon, & Philpott, 1981; Jain & Shore, 2006), we observed that combined auditory-somatosensory stimulation generally suppressed neural responses to auditory stimuli and that this suppression was most prominent in the LC matrix. Mechanistically, it is not known if such suppressive responses are created in the LC or are inherited from other brain regions since auditory-somatosensory interactions occur as early in the cochlear nucleus, and are also found in the IC, thalamus, and cortex (Aitkin et al., 1981; Haenggeli, Pongstaporn, Doucet, & Ryugo, 2005; Kimura, Imbe, Donishi, & Tamai, 2007; Li & Mizuno, 1997; Lohse, Dahmen, Bajo, & King, 2021; Shore, 2005; Shore, Vass, Wys, & Altschuler, 2000; C. Wong, Chabot, Kok, & Lomber, 2015), reviewed in (Brunelle & Llano, 2023; Lohse et al., 2022). We note that a systematic exploration of the stimulus space was not conducted here such that other acoustic or somatosensory stimuli, different relative amplitudes

or timings could have produced enhancement rather than suppression. Future work will be needed to further explore this stimulus space to more fully understand multisensory processing in the LC.

Conclusions:

Here, using a novel microprism approach to image the LC in anesthetized and awake mice, we observed that 1) DC displayed tonotopic organization which was not consistently present in the LC, 2) DC neurons were generally more sound-responsive than LC neurons but that neurons in both regions had preferential responses to spectrally- and temporally-complex stimuli, 3) that matrix regions of the LC were more responsive to spectrally- and temporally-complex stimuli than modules and that modules were more responsive to somatosensory stimuli and 4) that bimodal stimulation led to suppressive responses that were more prominent in the matrix and enhancement that was more prominent in modules. These data highlight significant organizational differences between the LC and DC and between modules and matrix in the LC. Future work using microprisms in the LC will help to reveal the potential differential role of matrix vs. module neurons in multisensory integration tasks in behaving animals.

Materials and methods:

Animal subjects:

Male mice of 8-12 weeks of age were used. Males were used as our preliminary data suggest male/female differences in DC organization (Ibrahim, Shinagawa, Xiao, Asilador, & Llano, 2022) and will be published separately. GAD67-GFP knock-in mice (developed and shared with permission from Dr. Yuchio Yanagawa at Gunma University and obtained from Dr. Douglas Oliver at the University of Connecticut), where GFP is exclusively expressed in GABAergic cells (Tamamaki et al., 2003), were used to visualize the GABAergic cells and LC modules. To simultaneously monitor calcium signals and visualize the GFP+ cells, Tg(Thy1-

468 jRGECO1a)GP8.20Dkim/J mice (Jackson Laboratory, Stock# 030525) were crossed with
469 GAD67-GFP knock-in mice to generate GAD67-GFPxThy1-jRGECO1a hybrid mice. The mice
470 were housed and bred at the animal research facility of The Beckman Institute for Advanced
471 Science and Technology. The animal care facilities are approved by the Association for
472 Assessment and Accreditation of Laboratory Animal Care (AAALAC). To phenotype the GFP-
473 positive animals, a single-photon fluorescence microscope was used for the transcranial
474 examination of the pups at postnatal day 4 using excitation: 472/30 nm and emission 520/35 nm
475 filters along with dichroic 505 nm long pass at low power magnification (2.5x/0.08, Olympus
476 objective, MPlanFL N, Japan). The positive pups exhibited a green fluorescence in the
477 cerebellum, the cerebral cortex, and the olfactory bulb and were only kept with their parents until
478 weaning. The genotyping for jRGECO1a was done using a probe composed of a forward
479 primer: GCCGCCGAGGTCAAGA & a reverse primer: TCCAACTTGATGTCGACGATGTAG) by
480 Transnetyx™ (Transnetyx, USA). Samples of the mice's tail snip around one month of age were
481 used for genotyping. All applicable guidelines for the care and use of animals were followed. All
482 procedures were approved by the Institutional Animal Care and Use Committee (IACUC).

483 **Surgery**

484 The general procedures of craniotomy were previously described (Goldey et al., 2014), with
485 modifications to place craniotomy over the IC. Before surgery, mice were anesthetized with a
486 mixture of ketamine, xylazine, and acepromazine (100 mg/kg, 3 mg/kg, and 3mg/kg,
487 respectively) delivered intraperitoneally. The anesthesia was maintained during the surgery and
488 imaging using only ketamine (100 mg/kg). To prevent neural edema during or after the
489 craniotomy, an intramuscular injection of dexamethasone sodium (4.8 mg/kg) was given just
490 before the surgery using an insulin syringe. After placing the animal in the stereotaxic apparatus
491 (David Kopf Instruments, USA), both eyes were protected by applying Optixcare lubricant eye
492 gel (Aventix Animal Health, Canada). The hair on the scalp was then removed by massaging

493 the scalp with a depilatory cream (Nair) using a cotton-tipped applicator and leaving the cream
494 on the scalp for 4-5 minutes. The cream was then removed by a thin plastic sheet (flexible ruler)
495 to leave a hair-free area on the scalp**.** The remaining tiny hairs were then removed by alcohol
496 swab and the area was then sterilized by applying 10% Povidone Iodine (Dynarex, USA) using
497 a sterile cotton-tipped applicator. The medial incision was made with a scalpel blade #10, and
498 0.2 ml of 0.5% lidocaine was injected intradermally into the scalp. The skin extending from the
499 medial line to the temporalis muscle was completely removed using a pair of microscissors to
500 produce a wide skinless area above the skull. Number 5/45 forceps were used to remove any
501 remaining periosteum. The remaining dried or firmly attached pieces of periosteum were
502 removed with a scalpel blade #10. The skull was cleaned with sterile saline and dried with
503 gently pressurized air. Using the stereotaxic apparatus, a wide area of ~3 x 4 mm above the left
504 IC was made. A micro drill bit (size #80, Grainger, USA) was used to drill through the skull
505 starting from the rostrolateral (Figure 1A, yellow circle) region to lambda (Figure 1A, black circle)
506 following the border in a clockwise direction (Figure 1A, dotted black rectangle). To prevent
507 overheating of the superficial brain tissues and to mitigate the occasional spurts of skull
508 bleeding during the drilling, ice-cold sterile saline was used to intermittently irrigate the surface.
509 A stream of pressurized air was also applied during the drilling procedures to prevent
510 overheating and remove the debris produced by the drilling. Caution was taken not to pierce the
511 dura when performing the craniotomy while crossing the sagittal or the lambdoid sutures to
512 avoid damaging the underlying sinuses. After drilling, the skull was irrigated in sterile saline and
513 the bone flap (the undrilled bone over the craniotomy area) was gently examined for complete
514 separation from the rest of the skull (Figure 1B). Using a pair of no. 5/45 forceps, the bone flap
515 was gently removed. To control the bleeding if it occurred, a piece of sterile hemostatic gel
516 (Adsorbable Gelatin Sponge USP, Haemosponge, GBI, India) which was pre-soaked in ice-cold
517 saline, was applied to the bleeding spot. Once the bleeding ceased, the brain was kept covered
518 in sterile saline. In some surgeries, the dura was peeled off from the surface of the IC while

519 removing the bone flap. In the surgeries where the dura remained intact, a Bonn microprobe
520 (F.S.T, Germany, Item # 10032-13) was used to pierce the dura in an area that is not above the
521 IC and devoid of cortical vasculature (e.g., a part of exposed cerebellum). After piercing, the
522 dura was carefully and gently lifted, and a pair of no. 5/45 forceps were used to grab the dura to
523 gently tear it to the extent of the transverse sinus to avoid bleeding of the major venous
524 structures.

525 Using the stereotaxic apparatus, a 30° diamond knife (F.S.T, Germany, Item # 10100-30) was
526 placed in its vertical position. From the medial line, the knife was placed at the lateral horizon of
527 the IC. The knife was then inserted 1.5 mm ventrally. Caution was taken to avoid hitting any
528 major blood vessels to avoid bleeding. From its position, the knife was retracted 0.3-0.5 mm
529 medially to create an initial pocket for the insertion of the microprism (Figures 1C-E). The
530 microprism (1.5 mm-silver coated, Tower Optical Corporation) was then inserted, so one of its
531 sides was parallel to the lateral surface of the diamond blade, the other side was facing up, and
532 its hypotenuse was facing ventrally (Figures 1F and G). The wooden piece of a cotton swab was
533 carefully driven down to push the microprism until its top surface was at the same level as the
534 IC dorsal surface. Keeping the microprism in its place with the wooden end of a swab, the
535 diamond knife was carefully retracted upward leaving the microprism behind (Figure 1H). If the
536 retraction of the diamond knife pulled the prism up, the wooden piece would be used to push it
537 down simultaneously with the knife movement. To control the bleeding, a piece of sterile
538 hemostatic gel was used as before. The tip of the diamond knife was used to secure the
539 microprism in its position for at least 10 minutes (Figure J). During that time, the solution of the
540 1% agarose was prepared for use. A pair of forceps were then used to gently place a sterile 5
541 mm cover glass #1 (Thomas Scientific, USA) over the skull covering the opened area above the
542 IC. The cover glass was secured by a wooden trimmed piece of sterile cotton swab by gently
543 pressing the cover glass from the top. Since the surface of the IC was located below the

544 surfaces of both the cerebellum and cerebral cortex, the cover glass usually traps about a 0.7-
545 1.0 mm thick sheet of sterile saline. The movement of the liquid medium caused by heart
546 pulsation was found to be a source of motion artifact during imaging, so the gap between the
547 surface of the IC and the cover glass was filled with 1% agarose gel that was made in saline at
548 a temperature range of 33-35°C (Figure 1K). The extra agarose gel pieces were cut off and
549 removed by the scalpel blade and the wet skull was then dried out using pressurized air. A
550 titanium headpost as described before (Goldey et al., 2014) was glued carefully on the top of
551 the skull to be at the same level as the cover glass. Following the manufacturer's instructions,
552 the C&B Metabond (Parkell, Japan) was used to secure the headpost in its place. Excluding the
553 steps of the microprism insertion, the same procedures were followed for DC imaging from the
554 surface (Figure 1L). For awake preparations, the same procedures were followed under
555 isoflurane anesthesia starting with 4% of isoflurane as an induction dose with 1-2% isoflurane
556 during the surgery. The animal was transferred under the microscope objective and left to
557 recover from isoflurane anesthesia for 1 hour before imaging. To ensure the animal's recovery,
558 the animal was visually inspected for its breathing rate (Ewald, Werb, & Egeblad, 2011) and for
559 ongoing limb movements.

560 **Acoustic stimulation:**

561 Using a custom-made MATLAB (The MathWorks, Natick, MA, USA) code, either 500 ms pure
562 tone or AM-noise was generated. Thirty-five (5x7) pure tones with a series of sound pressure
563 levels (40, 50, 60, 70, 80 dB SPL) and a series of carrier frequencies (5000-40000 Hz with a
564 half-octave gap) were presented with a cosine window. Forty-five (5x9) 100% AM white noise
565 bursts with a series of sound pressure levels (40, 50, 60, 70, 80 dB SPL) and modulation
566 frequencies (0, 2, 4, 8, 16, 32, 64, 128, 256 Hz) were generated. The stimuli of either pure tone
567 or AM-noise combinations were played in random sequence to the mice with a 600 ms
568 interstimulus interval (ISI) by a TDT RP2.1 processor (Tucker-Davis Technologies, US) and

delivered by a TDT ES1 speaker (Tucker-Davis Technologies, US). In other sets of experiments, 500 ms of nonmodulated broadband noise was presented 5 times with ISI of 600 ms at 80 dB SPL to examine the acoustic activity between modules and matrix compared to somatosensory stimulation.

The output of the TDT ES1 speaker was calibrated using a PCB 377A06 microphone, which feeds a SigCal tool to generate a calibration file for all tested frequencies (5–40 kHz). To enable the custom-made MATLAB code to read this calibration file, the values were first processed by MATLAB signal processing toolbox (sptool) to generate a 256-tap FIR filter to apply the calibration using the following parameters [arbitrary magnitudes, least square, order: 256, sampling rate: 97,656.25, frequency vector (5–40 kHz), amplitude vector (40–80 dB SPL), and weight vector ones (1128)].

Somatosensory stimulation:

The somatosensory stimulation was done by deflecting the right whiskers of the animals at an average excursion of 1.2 mm with a 50 Hz rate over 500 ms to match the acoustic stimulus. A total of five stimuli were presented with 600 ms ISI. The whisker deflection was performed using a Brüel & Kjær vibrator (V203 10/32 UNF- CE, United Kingdom) that was driven by a wave generator (4063, BK precision, USA) after amplifying the signals with an SLA1 100 W power amplifier (ART, USA).

Two-Photon imaging:

Immediately after surgery, the anesthetized animal was taken and secured under the microscope objective by clamping the arms of the head post to two perpendicular metal posts mounted on the microscope stage. A custom-built 2P microscope was used. The optical and the controlling components were supplied from Bruker, Olympus, and Thorlabs. The imaging of the DC was made using a 20x water-immersion objective (LUMPlanFI/IR, 20X, NA: 0.95, WD: 2

593 mm; Olympus Corporation, Tokyo, Japan), while the lateral surface of the IC was imaged by the
594 long working distance 16x water-immersion objective (N16XLWD-PF - CFI LWD Plan Fluorite
595 Objective, 16X, NA: 0.8, WD: 3.0 mm; Nikon, Tokyo, Japan) to be able to reach the focal point
596 of the microprism at its hypotenuse. For imaging both the GFP or jRGECO1a signals, the
597 excitation light was generated by InSight X3 laser (Spectra-Physics Lasers, Mountain View, CA,
598 USA) tuned to a wavelength of 920 or 1040 nm, respectively. A layer of a 1:1 mixture of
599 wavelength multipurpose ultrasound gel (National Therapy, Canada) with double deionized
600 water was used to immerse the objective. This gel was able to trap the water and reduce its
601 evaporation during imaging. The emitted signals were detected by a photomultiplier tube
602 (Hamamatsu H7422PA-4, Japan) following a t565lp dichroic and a Chroma barrier et525/70m
603 filter for GFP and et595/50m filter for jRGECO1a signals. Images (512x512 pixels) were
604 collected at a frame rate of 29.9 Hz in the resonant galvo mode. Data were collected from the
605 dorsal surface of the IC by scanning the surface of the IC based on the GFP and jRGECO1a
606 signals through the medial and lateral horizons of the IC. Generally, the scanning was started by
607 moving the 20x objective to the most ventromedial position, where there is no ability to see any
608 cells (Figure 2B, medial horizon). Then, the objective was started to slowly move dorsolaterally
609 to get cells in focus (Figure 1M), where the average depth of the first field of view was 169 μm.
610 The lateral movement of the objective was intended to be aligned and parallel to the curvature
611 of the DC surface indicated by getting the superficial cells in focus to avoid any possibility of
612 imaging the upper layers of the central nucleus of the IC, so the average depth of the most
613 superficial point of the imaging was 92 μm. The scanning was ended by moving the objective to
614 the most ventrolateral position of the IC, where there is no ability to see GFP laterally (Figure
615 2B, lateral horizon), where the last field of view was collected at an average depth of 225 μm.
616 Generally, each field of view was selected based on the expression of GFP signals as an
617 indicator for the cells in focus and being acoustically active by using a search stimulus that was

500 ms broadband noise with zero modulation at 80 dB SPL. The z-axis of the objective was determined relative to the pia surface. The relative position of each region was tracked through the micromanipulator (MP-285, Sutter Instruments) that controlled the microscope objective. The positions of imaged areas were further aligned across animals to a common coordinate using the midline, lateral extremes, and the vasculature landmarks taken via imaging of the GFP signals of the cranial window with low magnification (4x Olympus objective, 4x4 binning, 50 ms frame time) using a Lumen 200 bulb (Prior Scientific Inc, USA) and CoolSNAP MYO camera (Photometrics, USA, excitation: 488 nm and emission: 515–550 nm). Imaging of the lateral surface of the IC via microprism was done similarly. In both cases, the frame timing of the scanner and the sound stimuli were both digitized and time-locked using a Digidata 1440A (Molecular Devices, Sunnyvale, CA, USA) with Clampex v. 10.3 (Molecular Devices, Sunnyvale, CA, USA).

Laser lesion:

The laser lesion was produced using a 720 or 820 nm laser beam at 74-80 mW power at the level of the objective for 100 to 250 seconds depending on the size of the lesioned area, the speed of laser scanning (frame rate), and the depth of the lesion (z-axis length). In brief, the area of interest and the dimension of the laser lesion were initially determined using 920 nm as indicated by the GFP signals through scanning one of the GABAergic modules. The depth of the GABAergic modules was then determined by counting the optical slices starting from their superficial surface. The tunable laser was then switched from 920 nm to the shorter wavelength (720 or 820 nm) to scan the same area and depth at a rate (1-2 frames/ second).

Data processing:

Data collection: The data were collected as separate movies (512x512 pixels) for each pure tone or AM-noise runs in a resonant galvo mode. Depending on the amplitude and frequency combinations for each type of acoustic stimulus, 40- or 52-second periods were assigned as a

movie's length for pure tone (35 stimulus combinations), or AM-noise (45 stimulus combinations), respectively. Using ImageJ software, the z-projection was used to compute one single image representing either the sum, the standard deviation, or the median of all the image sequences in the movie. Based on these single images, the region of interest (ROI) was manually drawn around each detectable cell body. Figures 3A and B represent the sum of the images sequences of the movie collected from the dorsal surface, or the lateral surface of the IC via microprism, respectively. For the subsequent processing steps, Python open-source libraries were used (listed below).

Motion Correction and Filtering: The imread function from the OpenCV library was used in grayscale mode to import images into a numpy array from a single folder containing TIFF images. The array was then exported as a single TIFF stack into a temporary folder using the mimwrite function from the imageio library, and the process was repeated for each folder. The NoRMCorre algorithm (Pnevmatikakis & Giovannucci, 2017) embedded in the CaImAn library (Giovannucci et al., 2019) was used to apply motion correction to each of the TIFF files. The data were then imported into a numpy array, rounded, and converted to 16-bit integers. The images were filtered using a 2D Gaussian filter with a sigma value of 1 (surface View) / 2 (prism View) in each direction, then a 1D Gaussian temporal filter with a sigma value of 2 was applied using the ndimage.gaussian_filter and ndimage.gaussian_filter1d function from the scipy library, respectively.

Data Extraction: The ROI sets, which were manually created using ImageJ, were imported using the read_roi_zip function from the read_roi library. The sets were then used to create two masks; one mask was used as a replica of the ROIs and the second mask was made around the original ROI (roughly four times larger in area). The smaller mask was applied to find the average pixel value within each ROI, while the larger mask was applied to find the average pixel

value of the neuropil. The neuropil correction was applied using the following equation (Akerboom et al., 2012);

$$\text{Corrected value} = \text{Date value} - (0.4 \text{ X Neuropil value})$$

To identify the calcium signals, Δf/f was calculated by using the following equation.

$$\frac{\Delta \mathrm{f}}{\mathrm{f}} = \frac{(\text{Date value} - \text{Background value})}{\text{Background value}}$$

where the background value is the slope estimating the background levels with fluorescence bleaching factored in. The data were then reorganized so that all segments with the same stimulus frequency and stimulus amplitude were grouped. The area under the curve (AUC) of the calcium signals of the excitatory responses only was then used as a metric to determine the magnitude of the response and for subsequent analysis (Berens et al., 2018; Overk, Rockenstein, Florio, Cheng, & Masliah, 2015).

Cell Flagging: The correlation coefficient between each of the trials was calculated using the stats. Pearson function from the scipy library. The average correlation coefficient was calculated for each stimulus frequency and stimulus amplitude. Similar to previous work (A. B. Wong & Borst, 2019), if the average correlation coefficient was above the threshold of 0.6, the cell was flagged as being responsive to that stimulus combination of frequency and amplitude, and the best tone and modulation frequencies were calculated for every cell (Barnstedt et al., 2015). Knowing the best tonal frequency (BTF) and modulation frequency (BMF) for each neuron enabled us to calculate the SMI and TMI at each sound level following these equations;

$$\text{SMI} = \frac{\text{Response to BTF} - \text{Response to unmodulated noise}}{\text{Response to BTF} + \text{Response to unmodulated noise}}$$

The SMI has values ranging from (-1 to 1). While neurons with values closer to 1 are more responsive to pure tone, neurons with values closer to -1 are more responsive to noise with no modulation.

$$\text{TMI} = \frac{\text{Response to BMF} - \text{Response to unmodulated noise}}{\text{Response of BMF} + \text{Response to unmodulated noise}}$$

Similarly, the TMI has values ranging from (-1 to 1). While neurons with values closer to 1 are more responsive to AM-noise, neurons with values closer to -1 are more responsive to noise with no modulation.

For the comparison between somatosensory and auditory responses, the threshold of 0.4 was used as a cutoff threshold to determine the responsive cells to each stimulation. The average response of each somatosensory, acoustic (500 ms of unmodulated noise), or simultaneous somatosensory and acoustic (bimodal) stimulation was then calculated for each responsive cell.

To examine the effect of somatosensory stimulation on auditory responses, the response index (RI) was calculated for the auditory-responsive cells using the following equation;

$$\text{RI} = \frac{\text{Auditory response to bimodal stimulation}}{\text{Auditory response to auditory stimulation only}}$$

Reurons with RI values > 1 have enhanced or higher responses induced by simultaneous auditory and somatosensory stimulation, while neurons with RI values < 1 have downregulated or suppressed auditory responses induced by auditory and simultaneous somatosensory stimulation.

Map Generation: The average radius for all ROIs was calculated to ensure that all cells on the tonotopic map had uniform radii. A color key was also generated for every corresponding map.

705 A blank canvas was generated using the Image module from the pillow library, and a circle was
706 created for each cell and filled with a corresponding color to its value.

707 **Statistics:**

708 All statistical analyses and graphs were made using Origin Pro 2022 software. The normality of
709 the distributions of the data was examined using a Kolmogorov-Smirnov test. The Mann-
710 Whitney test as well as two-sample or paired t-test were used to examine the difference in data
711 distribution or the difference between samples of non-normal and normal distribution,
712 respectively. Either one-way or two-way ANOVA as well as Fisher as a post hoc test were used
713 for the mean comparison between different groups of normal distribution. The Chi-square (χ^2)
714 test was used to compare the samples based on cell numbers of their cellular population. The
715 cumulative frequency function was computed to calculate the fraction of cells tuned at each
716 frequency based on their best frequency. Differences were deemed significant when p-value
717 <0.05. The upper and lower borders of the each box plot are at the 25th and 75th percentile, with
718 whiskers at 95% spread.

719 **Histology:**

720 After the 2P imaging, the mouse was transcardially perfused with 4% paraformaldehyde (PFA)
721 solution in PBS solution. The isolated brain was then placed overnight in PFA for a complete
722 fixation. The brain was then moved from the PFA to a graded sucrose solution (10, 20, and
723 30%) until it sunk. 50 μm coronal sections were taken at the level of the IC using a Leica
724 cryostat. The sections were then mounted on a slide, coverslipped, and imaged using an
725 confocal microscope for imaging the GFP signals as an indicator for the GABAergic cells in the
726 GAD67-GFP knock-in mouse (excitation: 488 nm and emissions: 515–550 nm).

727 **Artwork:**

728 The cartoon of the mouse brain in Figures 1 C, F, and I was obtained from Brain Explorer 3D
729 viewer Allen Mouse Brain (https://connectivity.brain-map.org/3d-viewer?v=1) and modified to be
730 suitable for illustration. All figures were designed and made using Adobe Illustrator (Adobe, San
731 Jose, CA). To keep working within the Adobe environment to avoid losing the resolution of the
732 figures, Adobe Photoshop (Adobe, San Jose, CA) was used to crop the borders of some images
733 to save space.

734 **Acknowledgment**

735 We thank Dr. Kush Paul (Bruker) for initial training on the craniotomy surgery, Dr. Jason
736 Maclean (The Department of Neurobiology, University of Chicago) for assistance with 2P
737 imaging, Dr. Michael Jacobs Goard (Neuroscience Research Institute, The University of
738 California- Santa Barbara) for his guidance in the use of microprisms, Dr. Taher Saif
739 (Department of Mechanical Science and Engineering, The University of Illinois Urbana-
740 Champaign) for measuring the deflecting distance of the somatosensory stimulating probe using
741 a high-speed camera, and Dr. Pengfei Song (Department of Electric and Computer Engineering,
742 The University of Illinois Urbana-Champaign) for his assistance with the somatosensory
743 stimulating probe. We also thank the NIDCD for funding this work under grant # R01DC013073
744 and R01DC016599.

745 **Competing interests**

746 On behalf of all authors, there are no financial or non-financial competing interests to be
747 declared.

748 **References**

749 Aitkin, L. M., Dickhaus, H., Schult, W., & Zimmermann, M. (1978). External nucleus of inferior colliculus:
750 auditory and spinal somatosensory afferents and their interactions. *J Neurophysiol, 41*(4), 837-
751 847. doi:10.1152/jn.1978.41.4.837

Aitkin, L. M., Kenyon, C. E., & Philpott, P. (1981). The representation of the auditory and somatosensory systems in the external nucleus of the cat inferior colliculus. *J Comp Neurol, 196*(1), 25-40. doi:10.1002/cne.901960104

Akerboom, J., Chen, T. W., Wardill, T. J., Tian, L., Marvin, J. S., Mutlu, S., . . . Looger, L. L. (2012). Optimization of a GCaMP calcium indicator for neural activity imaging. *J Neurosci, 32*(40), 13819-13840. doi:10.1523/JNEUROSCI.2601-12.2012

Alexander, G. E., Crutcher, M. D., & DeLong, M. R. (1990). Basal ganglia-thalamocortical circuits: parallel substrates for motor, oculomotor, "prefrontal" and "limbic" functions. *Prog Brain Res, 85*, 119-146.

Andermann, M. L., Gilfoy, N. B., Goldey, G. J., Sachdev, R. N., Wölfel, M., McCormick, D. A., . . . Levene, M. J. (2013). Chronic cellular imaging of entire cortical columns in awake mice using microprisms. *Neuron, 80*(4), 900-913. doi:10.1016/j.neuron.2013.07.052

Bajo, V. M., & Moore, D. R. (2005). Descending projections from the auditory cortex to the inferior colliculus in the gerbil, Meriones unguiculatus. *J Comp Neurol, 486*(2), 101-116. doi:10.1002/cne.20542

Bandyopadhyay, S., Shamma, S. A., & Kanold, P. O. (2010). Dichotomy of functional organization in the mouse auditory cortex. *Nat Neurosci, 13*(3), 361-368. doi:10.1038/nn.2490

Barnstedt, O., Keating, P., Weissenberger, Y., King, A. J., & Dahmen, J. C. (2015). Functional Microarchitecture of the Mouse Dorsal Inferior Colliculus Revealed through In Vivo Two-Photon Calcium Imaging. *J Neurosci, 35*(31), 10927-10939. doi:10.1523/JNEUROSCI.0103-15.2015

Beckmann, L., Zhang, X., Nadkarni, N. A., Cai, Z., Batra, A., Sullivan, D. P., . . . Zhang, H. F. (2019). Longitudinal deep-brain imaging in mouse using visible-light optical coherence tomography through chronic microprism cranial window. *Biomed Opt Express, 10*(10), 5235-5250. doi:10.1364/BOE.10.005235

Berens, P., Freeman, J., Deneux, T., Chenkov, N., McColgan, T., Speiser, A., . . . Bethge, M. (2018). Community-based benchmarking improves spike rate inference from two-photon calcium imaging data. *PLoS Comput Biol, 14*(5), e1006157. doi:10.1371/journal.pcbi.1006157

Brimblecombe, K. R., & Cragg, S. J. (2017). The Striosome and Matrix Compartments of the Striatum: A Path through the Labyrinth from Neurochemistry toward Function. *ACS Chem Neurosci, 8*(2), 235-242. doi:10.1021/acschemneuro.6b00333

Brunelle, D. L., & Llano, D. A. (2023). Role of auditory-somatosensory corticothalamic circuit integration in analgesia. *Cell Calcium, 111*, 102717. doi:10.1016/j.ceca.2023.102717

Cai, D., Han, R., Liu, M., Xie, F., You, L., Zheng, Y., . . . Yuan, K. (2018). A Critical Role of Inhibition in Temporal Processing Maturation in the Primary Auditory Cortex. *Cereb Cortex, 28*(5), 1610-1624. doi:10.1093/cercor/bhx057

Chang, E. F., Bao, S., Imaizumi, K., Schreiner, C. E., & Merzenich, M. M. (2005). Development of spectral and temporal response selectivity in the auditory cortex. *Proc Natl Acad Sci U S A, 102*(45), 16460-16465. doi:10.1073/pnas.0508239102

Chen, C., Cheng, M., Ito, T., & Song, S. (2018). Neuronal Organization in the Inferior Colliculus Revisited with Cell-Type-Dependent Monosynaptic Tracing. *J Neurosci, 38*(13), 3318-3332. doi:10.1523/JNEUROSCI.2173-17.2018

Chernock, M. L., Larue, D. T., & Winer, J. A. (2004). A periodic network of neurochemical modules in the inferior colliculus. *Hear Res, 188*(1-2), 12-20. doi:10.1016/S0378-5955(03)00340-X

Chia, T. H., & Levene, M. J. (2009). Microprisms for in vivo multilayer cortical imaging. *J Neurophysiol, 102*(2), 1310-1314. doi:10.1152/jn.91208.2008

Coleman, J. R., & Clerici, W. J. (1987). Sources of projections to subdivisions of the inferior colliculus in the rat. *J Comp Neurol, 262*(2), 215-226. doi:10.1002/cne.902620204

Dana, H., Novak, O., Guardado-Montesino, M., Fransen, J. W., Hu, A., Borghuis, B. G., . . . Svoboda, K. (2018). Thy1 transgenic mice expressing the red fluorescent calcium indicator jRGECO1a for neuronal population imaging in vivo. *PLoS One, 13*(10), e0205444. doi:10.1371/journal.pone.0205444

Davis, K. A., Ramachandran, R., & May, B. J. (2003). Auditory processing of spectral cues for sound localization in the inferior colliculus. *J Assoc Res Otolaryngol, 4*(2), 148-163. doi:10.1007/s10162-002-2002-5

Dillingham, C. H., Gay, S. M., Behrooz, R., & Gabriele, M. L. (2017). Modular-extramodular organization in developing multisensory shell regions of the mouse inferior colliculus. *J Comp Neurol, 525*(17), 3742-3756. doi:10.1002/cne.24300

DL, Oliver. (2005). Neuronal organization in the inferior colliculus. In Winer JA & Schreiner CE (Eds.), *The inferior colliculus.* (pp. 69–114). New York: Springer.

Draganski, B., Kherif, F., Klöppel, S., Cook, P. A., Alexander, D. C., Parker, G. J., . . . Frackowiak, R. S. (2008). Evidence for segregated and integrative connectivity patterns in the human Basal Ganglia. *J Neurosci, 28*(28), 7143-7152. doi:10.1523/JNEUROSCI.1486-08.2008

Ewald, A. J., Werb, Z., & Egeblad, M. (2011). Monitoring of vital signs for long-term survival of mice under anesthesia. *Cold Spring Harb Protoc, 2011*(2), pdb.prot5563. doi:10.1101/pdb.prot5563

Fair, D. A., Dosenbach, N. U., Church, J. A., Cohen, A. L., Brahmbhatt, S., Miezin, F. M., . . . Schlaggar, B. L. (2007). Development of distinct control networks through segregation and integration. *Proc Natl Acad Sci U S A, 104*(33), 13507-13512. doi:10.1073/pnas.0705843104

Faye-Lund, H., & Osen, K. K. (1985). Anatomy of the inferior colliculus in rat. *Anat Embryol (Berl), 171*(1), 1-20. doi:10.1007/BF00319050

Frisina, R. D. (2001). Subcortical neural coding mechanisms for auditory temporal processing. *Hear Res, 158*(1-2), 1-27. doi:10.1016/s0378-5955(01)00296-9

Gerfen, C. R. (1985). The neostriatal mosaic. I. Compartmental organization of projections from the striatum to the substantia nigra in the rat. *J Comp Neurol, 236*(4), 454-476. doi:10.1002/cne.902360404

Giovannucci, A., Friedrich, J., Gunn, P., Kalfon, J., Brown, B. L., Koay, S. A., . . . Pnevmatikakis, E. A. (2019). CaImAn an open source tool for scalable calcium imaging data analysis. *Elife, 8*. doi:10.7554/eLife.38173

Goldey, G. J., Roumis, D. K., Glickfeld, L. L., Kerlin, A. M., Reid, R. C., Bonin, V., . . . Andermann, M. L. (2014). Removable cranial windows for long-term imaging in awake mice. *Nat Protoc, 9*(11), 2515-2538. doi:10.1038/nprot.2014.165

Goodman, D. F., Benichoux, V., & Brette, R. (2013). Decoding neural responses to temporal cues for sound localization. *Elife, 2*, e01312. doi:10.7554/eLife.01312

Haenggeli, C. A., Pongstaporn, T., Doucet, J. R., & Ryugo, D. K. (2005). Projections from the spinal trigeminal nucleus to the cochlear nucleus in the rat. *J Comp Neurol, 484*(2), 191-205. doi:10.1002/cne.20466

Heys, J. G., Rangarajan, K. V., & Dombeck, D. A. (2014). The functional micro-organization of grid cells revealed by cellular-resolution imaging. *Neuron, 84*(5), 1079-1090. doi:10.1016/j.neuron.2014.10.048

Ibrahim, Baher, Shinagawa, Yoshitaka, Xiao, Gang, Asilador, Alexander, & Llano, Daniel. (2022). *Using Microprisms, the 2P Calcium Imaging Revealed a Functional Distinction between the Dorsal & Lateral Cortices of the Mouse Inferior Colliculus.* Paper presented at the Association for Research in Otolaryngology, Virtual.

Ito, T., Hirose, J., Murase, K., & Ikeda, H. (2014). Determining auditory-evoked activities from multiple cells in layer 1 of the dorsal cortex of the inferior colliculus of mice by in vivo calcium imaging. *Brain Res, 1590*, 45-55. doi:10.1016/j.brainres.2014.09.049

Jain, R., & Shore, S. (2006). External inferior colliculus integrates trigeminal and acoustic information: unit responses to trigeminal nucleus and acoustic stimulation in the guinea pig. *Neurosci Lett, 395*(1), 71-75. doi:10.1016/j.neulet.2005.10.077

JF, Willott. (2001). Handbook of mouse auditory research. In Willott JF (Ed.), *Behavior to molecular biology*. Boca Raton, FL: CRC.

Joris, P. X., Schreiner, C. E., & Rees, A. (2004). Neural processing of amplitude-modulated sounds. *Physiol Rev, 84*(2), 541-577. doi:10.1152/physrev.00029.2003

Kasai, M., Ono, M., & Ohmori, H. (2012). Distinct neural firing mechanisms to tonal stimuli offset in the inferior colliculus of mice in vivo. *Neurosci Res, 73*(3), 224-237. doi:10.1016/j.neures.2012.04.009

Kimura, A., Imbe, H., Donishi, T., & Tamai, Y. (2007). Axonal projections of single auditory neurons in the thalamic reticular nucleus: implications for tonotopy-related gating function and cross-modal modulation. *Eur J Neurosci, 26*(12), 3524-3535. doi:10.1111/j.1460-9568.2007.05925.x

Lamb-Echegaray, I. D., Noftz, W. A., Stinson, J. P. C., & Gabriele, M. L. (2019). Shaping of discrete auditory inputs to extramodular zones of the lateral cortex of the inferior colliculus. *Brain Struct Funct, 224*(9), 3353-3371. doi:10.1007/s00429-019-01979-6

Langner, G. (1992). Periodicity coding in the auditory system. *Hear Res, 60*(2), 115-142. doi:10.1016/0378-5955(92)90015-f

Lesicko, A. M. H., & Geffen, M. N. (2022). Diverse functions of the auditory cortico-collicular pathway. *Hear Res, 425*, 108488. doi:10.1016/j.heares.2022.108488

Lesicko, A. M. H., Sons, S. K., & Llano, D. A. (2020). Circuit Mechanisms Underlying the Segregation and Integration of Parallel Processing Streams in the Inferior Colliculus. *J Neurosci, 40*(33), 6328-6344. doi:10.1523/JNEUROSCI.0646-20.2020

Lesicko, A. M., Hristova, T. S., Maigler, K. C., & Llano, D. A. (2016). Connectional Modularity of Top-Down and Bottom-Up Multimodal Inputs to the Lateral Cortex of the Mouse Inferior Colliculus. *J Neurosci, 36*(43), 11037-11050. doi:10.1523/JNEUROSCI.4134-15.2016

Li, H., & Mizuno, N. (1997). Single neurons in the spinal trigeminal and dorsal column nuclei project to both the cochlear nucleus and the inferior colliculus by way of axon collaterals: a fluorescent retrograde double-labeling study in the rat. *Neurosci Res, 29*(2), 135-142. doi:10.1016/s0168-0102(97)00082-5

Liu, M., Xie, F., Dai, J., Zhang, J., Yuan, K., & Wang, N. (2023). Brain-wide inputs to the non-lemniscal inferior colliculus in mice. *Neurosci Lett, 793*, 136976. doi:10.1016/j.neulet.2022.136976

Loftus, W. C., Malmierca, M. S., Bishop, D. C., & Oliver, D. L. (2008). The cytoarchitecture of the inferior colliculus revisited: a common organization of the lateral cortex in rat and cat. *Neuroscience, 154*(1), 196-205. doi:10.1016/j.neuroscience.2008.01.019

Lohse, M., Dahmen, J. C., Bajo, V. M., & King, A. J. (2021). Subcortical circuits mediate communication between primary sensory cortical areas in mice. *Nat Commun, 12*(1), 3916. doi:10.1038/s41467-021-24200-x

Lohse, M., Zimmer-Harwood, P., Dahmen, J. C., & King, A. J. (2022). Integration of somatosensory and motor-related information in the auditory system. *Front Neurosci, 16*, 1010211. doi:10.3389/fnins.2022.1010211

Low, R. J., Gu, Y., & Tank, D. W. (2014). Cellular resolution optical access to brain regions in fissures: imaging medial prefrontal cortex and grid cells in entorhinal cortex. *Proc Natl Acad Sci U S A, 111*(52), 18739-18744. doi:10.1073/pnas.1421753111

Marks, T. D., & Goard, M. J. (2021). Stimulus-dependent representational drift in primary visual cortex. *Nat Commun, 12*(1), 5169. doi:10.1038/s41467-021-25436-3

Nelson, P. C., & Carney, L. H. (2007). Neural rate and timing cues for detection and discrimination of amplitude-modulated tones in the awake rabbit inferior colliculus. *J Neurophysiol, 97*(1), 522-539. doi:10.1152/jn.00776.2006

Oliver, Douglas L. (2005). Neuronal Organization in the Inferior Colliculus. In J.A. Winer & C.E. Schreiner (Eds.), *The Inferior Colliculus.* New York, NY.: Springer.

Overk, C. R., Rockenstein, E., Florio, J., Cheng, Q., & Masliah, E. (2015). Differential calcium alterations in animal models of neurodegenerative disease: Reversal by FK506. *Neuroscience, 310*, 549-560. doi:10.1016/j.neuroscience.2015.08.068

Pnevmatikakis, E. A., & Giovannucci, A. (2017). NoRMCorre: An online algorithm for piecewise rigid motion correction of calcium imaging data. *J Neurosci Methods, 291*, 83-94. doi:10.1016/j.jneumeth.2017.07.031

Rabang, C. F., Parthasarathy, A., Venkataraman, Y., Fisher, Z. L., Gardner, S. M., & Bartlett, E. L. (2012). A computational model of inferior colliculus responses to amplitude modulated sounds in young and aged rats. *Front Neural Circuits, 6*, 77. doi:10.3389/fncir.2012.00077

Rees, A., & Langner, G. (2005). Temporal Coding in the Auditory Midbrain. In J.A. Winer & C.E. Schreiner (Eds.), *The Inferior Colliculus.* . New York, NY.: Springer.

Romand, R., & Ehret, G. (1990). Development of tonotopy in the inferior colliculus. I. Electrophysiological mapping in house mice. *Brain Res Dev Brain Res, 54*(2), 221-234. doi:10.1016/0165-3806(90)90145-o

Romero, S., Hight, A. E., Clayton, K. K., Resnik, J., Williamson, R. S., Hancock, K. E., & Polley, D. B. (2020). Cellular and Widefield Imaging of Sound Frequency Organization in Primary and Higher Order Fields of the Mouse Auditory Cortex. *Cereb Cortex, 30*(3), 1603-1622. doi:10.1093/cercor/bhz190

Rothschild, G., Nelken, I., & Mizrahi, A. (2010). Functional organization and population dynamics in the mouse primary auditory cortex. *Nat Neurosci, 13*(3), 353-360. doi:10.1038/nn.2484

Saldaña, E., Feliciano, M., & Mugnaini, E. (1996). Distribution of descending projections from primary auditory neocortex to inferior colliculus mimics the topography of intracollicular projections. *J Comp Neurol, 371*(1), 15-40. doi:10.1002/(SICI)1096-9861(19960715)371:1<15::AID-CNE2>3.0.CO;2-O

Schreiner, Christoph E, & Winer, Jeffery A. (2005). *The inferior colliculus*: Springer Science+ Business Media, Incorporated.

Shen, Junxian, Xu, Zhimin, & Shen, Lijian. (2003). Topography of acoustic response characteristics in the midbrain inferior colliculus of Kunming mouse. *<i data-test="journal-title" style="margin: 0px; box-sizing: inherit;">Chinese Science Bulletin volume, 48*, 161–165. doi:https://doi.org/10.1360/03tb9033

Shore, S. E. (2005). Multisensory integration in the dorsal cochlear nucleus: unit responses to acoustic and trigeminal ganglion stimulation. *Eur J Neurosci, 21*(12), 3334-3348. doi:10.1111/j.1460-9568.2005.04142.x

Shore, S. E., Vass, Z., Wys, N. L., & Altschuler, R. A. (2000). Trigeminal ganglion innervates the auditory brainstem. *J Comp Neurol, 419*(3), 271-285. doi:10.1002/(sici)1096-9861(20000410)419:3<271::aid-cne1>3.0.co;2-m

Sinex, D. G. (2005). Spectral processing and sound source determination. *Int Rev Neurobiol, 70*, 371-398. doi:10.1016/S0074-7742(05)70011-8

Singh, N. C., & Theunissen, F. E. (2003). Modulation spectra of natural sounds and ethological theories of auditory processing. *J Acoust Soc Am, 114*(6 Pt 1), 3394-3411. doi:10.1121/1.1624067

Solyga, M., & Barkat, T. R. (2021). Emergence and function of cortical offset responses in sound termination detection. *Elife, 10*. doi:10.7554/eLife.72240

Sporns, O., Tononi, G., & Edelman, G. M. (2000). Connectivity and complexity: the relationship between neuroanatomy and brain dynamics. *Neural Netw, 13*(8-9), 909-922. doi:10.1016/s0893-6080(00)00053-8

Stiebler, I., & Ehret, G. (1985). Inferior colliculus of the house mouse. I. A quantitative study of tonotopic organization, frequency representation, and tone-threshold distribution. *J Comp Neurol, 238*(1), 65-76. doi:10.1002/cne.902380106

Tamamaki, N., Yanagawa, Y., Tomioka, R., Miyazaki, J., Obata, K., & Kaneko, T. (2003). Green fluorescent protein expression and colocalization with calretinin, parvalbumin, and somatostatin in the GAD67-GFP knock-in mouse. *J Comp Neurol, 467*(1), 60-79. doi:10.1002/cne.10905

Tononi, G., Sporns, O., & Edelman, G. M. (1994). A measure for brain complexity: relating functional segregation and integration in the nervous system. *Proc Natl Acad Sci U S A, 91*(11), 5033-5037. doi:10.1073/pnas.91.11.5033

Vogelstein, J. T., Packer, A. M., Machado, T. A., Sippy, T., Babadi, B., Yuste, R., & Paninski, L. (2010). Fast nonnegative deconvolution for spike train inference from population calcium imaging. *J Neurophysiol, 104*(6), 3691-3704. doi:10.1152/jn.01073.2009

Wehr, M., & Zador, A. M. (2003). Balanced inhibition underlies tuning and sharpens spike timing in auditory cortex. *Nature, 426*(6965), 442-446. doi:10.1038/nature02116

Wenzel, M., Hamm, J. P., Peterka, D. S., & Yuste, R. (2017). Reliable and Elastic Propagation of Cortical Seizures In Vivo. *Cell Rep, 19*(13), 2681-2693. doi:10.1016/j.celrep.2017.05.090

Willard, F. H., & Ryugo, D. K. (1983). Anatomy of the central auditory system. In J. F. Willot (Ed.), *The auditory psychobiology of the mouse.* (pp. 201-304). Springfield, IL: Thomas.

Willard FH, & DK, Ryugo. (1983). Anatomy of the central auditory system. In Willott JF (Ed.), *The auditory psychobiology of the mouse.* (pp. 201-304). Springfield, IL: Thomas.

Willott, James F. (2001). *Handbook of Mouse Auditory Research From Behavior to Molecular Biology* (1st Edition ed.). Boca Raton: CRC Press.

Winer, J. A., Larue, D. T., Diehl, J. J., & Hefti, B. J. (1998). Auditory cortical projections to the cat inferior colliculus. *J Comp Neurol, 400*(2), 147-174.

Wong, A. B., & Borst, J. G. G. (2019). Tonotopic and non-auditory organization of the mouse dorsal inferior colliculus revealed by two-photon imaging. *Elife, 8*. doi:10.7554/eLife.49091

Wong, C., Chabot, N., Kok, M. A., & Lomber, S. G. (2015). Amplified somatosensory and visual cortical projections to a core auditory area, the anterior auditory field, following early- and late-onset deafness. *J Comp Neurol, 523*(13), 1925-1947. doi:10.1002/cne.23771

Xiong, B., Li, A., Lou, Y., Chen, S., Long, B., Peng, J., . . . Gong, H. (2017). Precise Cerebral Vascular Atlas in Stereotaxic Coordinates of Whole Mouse Brain. *Front Neuroanat, 11*, 128. doi:10.3389/fnana.2017.00128

Xu, Na Fu, Zi-Ying Chen, Qi-Cai. (2014). The function of offset neurons in auditory information processing. *Translational Neuroscience, 5*(4), 275-285. doi:https://doi.org/10.2478/s13380-014-0235-5

Yaksi, E., & Friedrich, R. W. (2006). Reconstruction of firing rate changes across neuronal populations by temporally deconvolved Ca2+ imaging. *Nat Methods, 3*(5), 377-383. doi:10.1038/nmeth874

Zhou, J., & Shore, S. (2006). Convergence of spinal trigeminal and cochlear nucleus projections in the inferior colliculus of the guinea pig. *J Comp Neurol, 495*(1), 100-112. doi:10.1002/cne.20863

Figure 1:

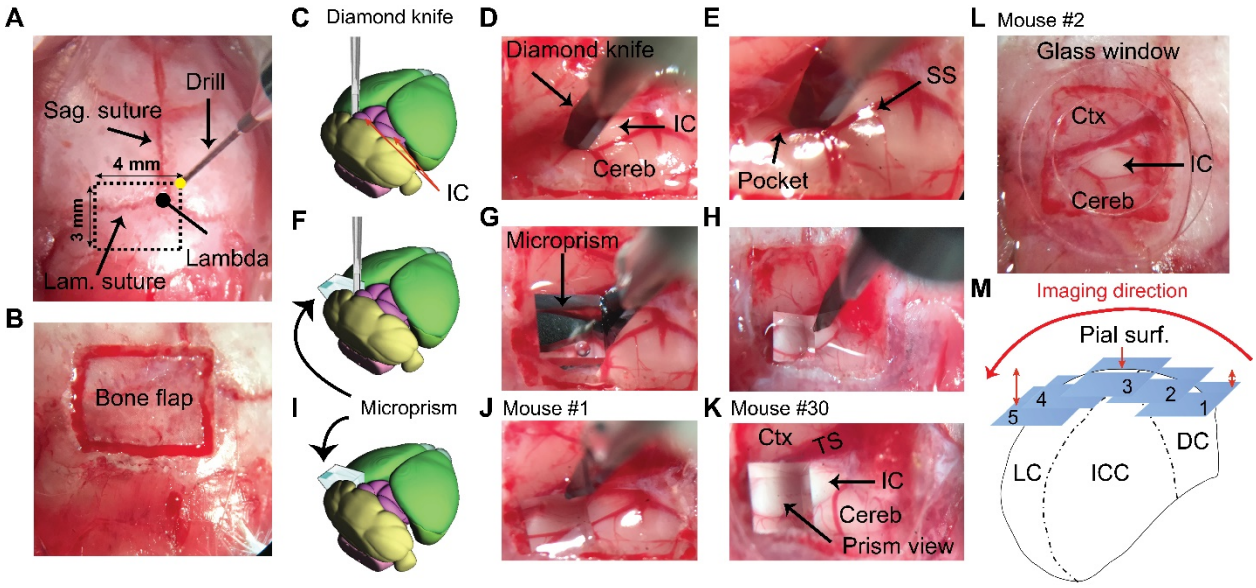

Figure 1: A brief Illustration of the surgical procedures.

(A) A surface view of the mouse's skull showing the landmarks of the craniotomy over the IC. (B) An image of the bone flap after finishing the drilling. (C-E) A cartoon and two images of the brain surface showing the insertion and the pocket made by the diamond knife at the lateral surface of the left IC. (F-H) A cartoon and two images of the brain surface showing the insertion of the microprism into its pocket to directly face the LC after displacing the blade of the diamond knife. (I-K) A cartoon and two images of the brain surface showing the final setup of the microprism for two different animals. (L) An image of the brain surface showing the placement of a glass window for the surface imaging of the DC. (M) A cartoon of the coronal section of the IC demonstrating the different fields of views taken along the mediolateral axis parallel to the curvature of the IC surface at different depths (1-5) from the pial surface. Cereb: Cerebellum, Ctx: Cerebral cortex, DC: Dorsal cortex of the IC, IC: Inferior colliculus, ICC: Central nucleus of the IC, Lam. Lambdoid, LC: Lateral cortex of the IC, Sag. Sagittal, SS: Sigmoid sinus, Surf: Surface, TS: Transverse sinus.

1002 **Figure 2:**

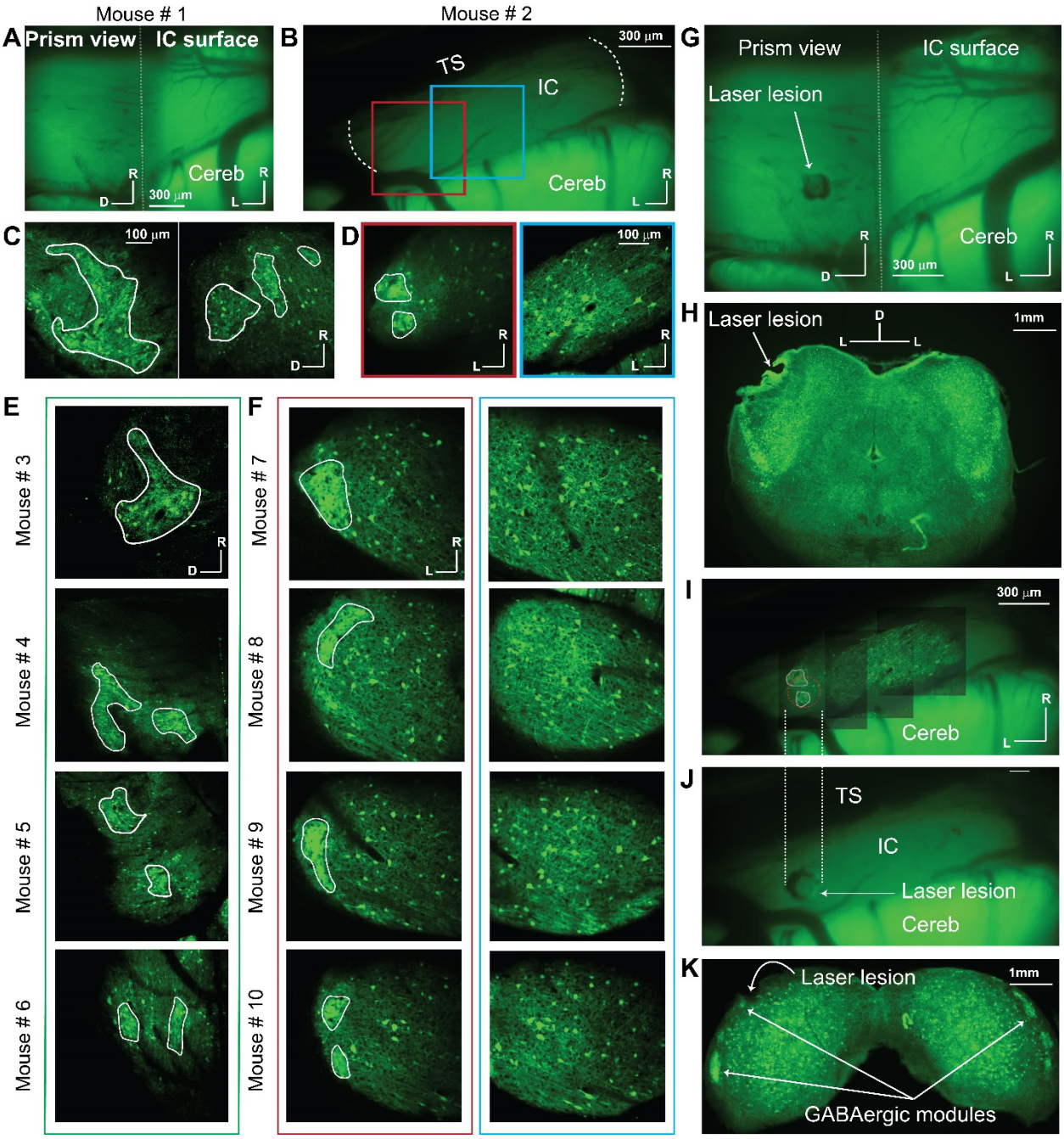

1003

1004 **Figure 2: The distribution of GABAergic cells on the LC imaged via microprism, and DC**

1005 **imaged from the dorsal surface.**

1006 All images were taken for the GFP signals exclusively expressed in GABAergic cells. (A-B) Low
1007 magnification of fluorescence images for the GFP signals obtained from the IC surface with or
1008 without the microprism, respectively. The dotted white line in B represented the medial and
1009 lateral horizons of the IC. (C-E) The 2P images of the GABAergic cells on the LC imaged via
1010 microprism showing the GABAergic modules across multiple animals. (D and F) The 2P images
1011 of the GABAergic cells on either the dorsolateral surface of the DC imaged directly from its
1012 dorsal surface showing the GABAergic modules across multiple animals (red boxes) or its
1013 dorsomedial surface showing a homogenous distribution of GABAergic cells of different sizes
1014 with no signs of the GABAergic modules across multiple animals (blue boxes). (G) A low
1015 magnification fluorescence image of the IC surface with the microprism showing a laser lesion
1016 spot made through the microprism to validate the position of the microprism relative to the IC.
1017 (H) A histological coronal section at the level of the IC showing that the laser lesion made by the
1018 microprism was located at the sagittal surface of the LC imaged via microprism. (I-J) Low-
1019 magnification fluorescence images of the IC surface from the dorsal surface show a laser lesion
1020 spot made on the dorsolateral surface of the LC on the GABAergic module. The dotted white
1021 lines represent the alignment of the laser lesion (dotted red circle) to the location of the
1022 GABAergic module at the dorsolateral surface. (K) A histological coronal section at the level of
1023 the IC showing that the laser lesion made on the IC surface targeted the GABAergic module at
1024 the dorsolateral portion of the LC. All solid irregular white lines were made at the border of the
1025 GABAergic modules; D: Dorsal, IC: Inferior colliculus, L: Lateral, R: Rostral. Cereb: Cerebellum,
1026 TS: Transverse sinus.

1027

1028

1029

1030 **Figure 3:**

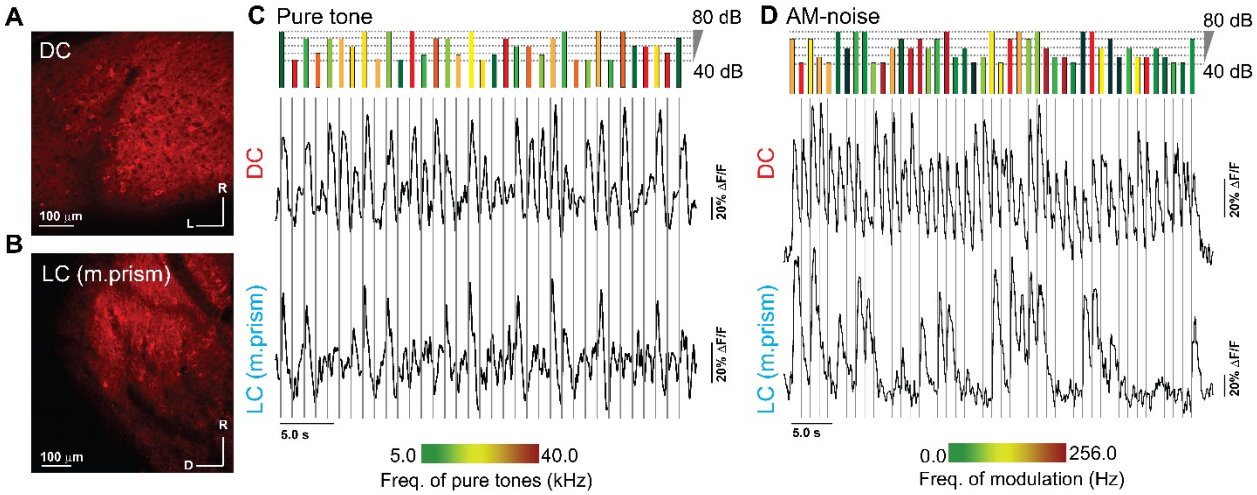

1031

1032 **Figure 3: 2P expression of jRGECO1a along with evoked signals in the DC imaged from**

1033 **the dorsal surface and LC imaged via microprism.**

1034 (A-B) The 2P images of the jRGECO1a expression on the DC imaged from the dorsal surface

1035 and the LC imaged via a microprism, respectively. (C-D) The time traces of the evoked calcium

1036 signals by either different frequencies and amplitudes of pure tones or different overall

1037 amplitudes and rates of AM of broadband noise, respectively, which were obtained from two

1038 different cells on the DC (top traces) or the LC imaged via microprism (bottom traces); The

1039 length of the colored bars (top) indicates the intensity of the stimulus, while the color indicates

1040 the tone or AM frequency depending on the color scale (bottom). AM-noise: Amplitude

1041 modulated broadband noise, D: Dorsal, DC: Dorsal cortex, L: Lateral, LC: Lateral cortex,

1042 m.prism: Microprism, R: Rostral.

1043

1044

1045

1046

1047 **Figure 4:**

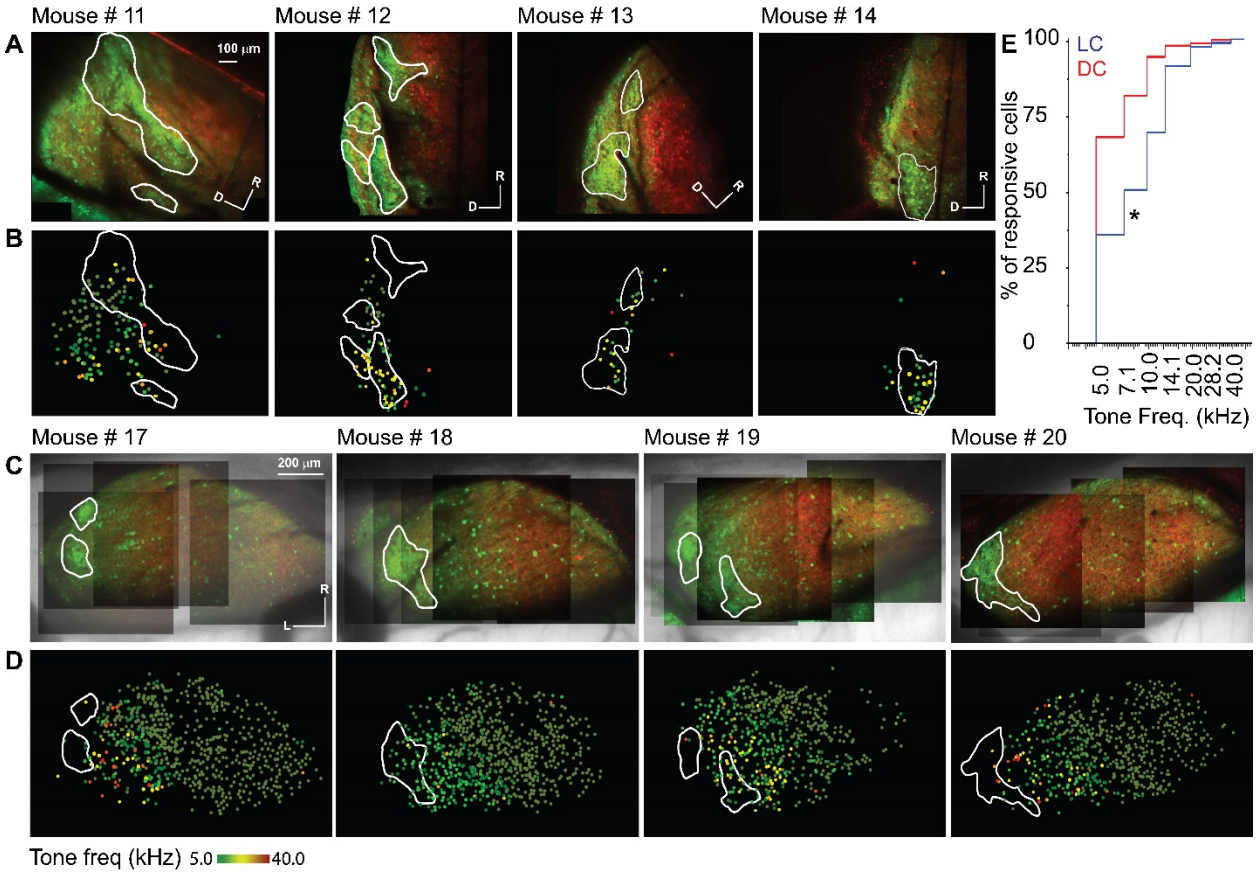

1048

1049 **Figure 4: The auditory cellular organization of the LC imaged via microprism vs. DC**

1050 **imaged from the dorsal surface.**

1051 (A and C) The 2P images of GFP (green) and jRGECO1a expression (red) on either the LC

1052 imaged via the microprism or the DC imaged from the dorsal surface, respectively. (B and D)

1053 The pseudocolor images show the responsive cells to the pure tone of different combinations of

1054 frequencies and levels on the surface of the LC imaged via the microprism or the DC imaged

1055 from its dorsal surface, respectively. (E) The cumulative distribution function of the best tone

1056 frequencies of all cells collected either from the LC imaged via microprism (blue line) or the DC

1057 imaged directly from its dorsal surface (red line). D: Dorsal, L: Lateral, R: Rostral. (*$p<0.05$, LC

1058 vs. DC).

1059 **Figure 5:**

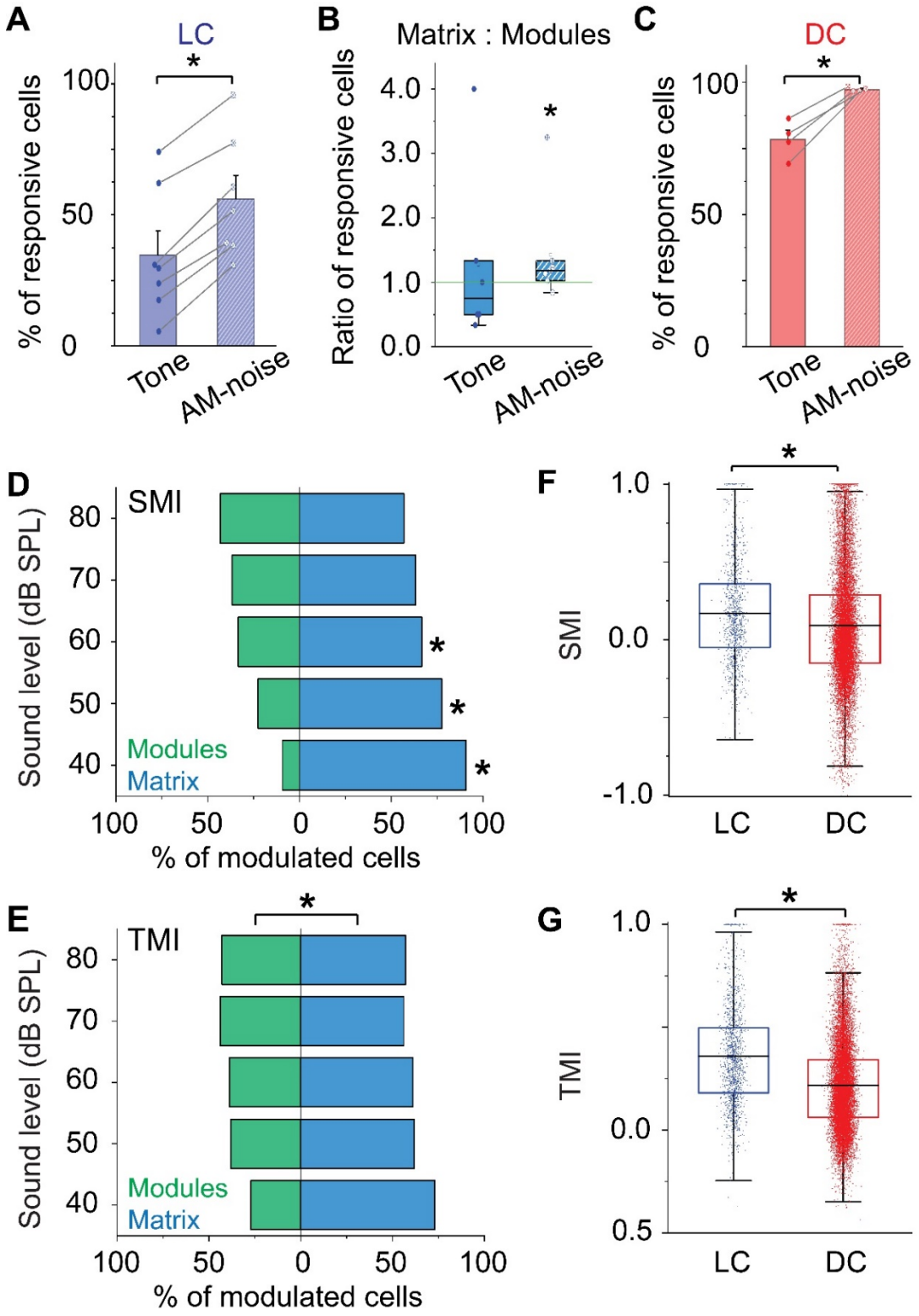

1060

Figure 5: The cellular response to pure tones and AM-noise of the LC imaged via microprism vs. DC imaged from the dorsal surface.

(A and C) Bar graphs showing the difference in the cellular response to pure tone (tone) vs. AM-noise on the LC imaged via microprism or the DC imaged directly from the dorsal surface, respectively (*p<0.05, pure tone vs. AM-noise). (B) A bar graph showing the difference in the cellular response to the pure tone (tone) and AM-noise of the matrix after normalization against modules imaged via microprism (*p<0.05, matrix vs. modules). (D and E) Bar graphs showing the percentage of spectrally (two-way ANOVA: $f_{(1, 4, 9)}$ = 50.3, 0.0, and 4.0 - p = $7.1x10^{-7}$, 1.0, and 0.01 for the region, sound level, and interaction, respectively, Fisher post hoc, p = $5.1x10^{-6}$, $4.9x10^{-4}$, 0.02, 0.058, and 0.14 for modules vs. matrix at 40, 50, 60, 70, and 80 dB, respectively) or temporally (two-way ANOVA: $f_{(1, 4, 9)}$ = 19.3, 0.0, and 1.2 - p = $7.1x10^{-7}$, 1.0, and 0.32 for the region, sound level, and interaction, respectively, Fisher post hoc, p = $2.7x10^{-7}$for modules vs. matrix) modulated cells, respectively, across different sound levels in modules (green bars) vs. matrix (blue bars) imaged via microprism. (*p<0.05, matrix vs. modules). (F and G) box plots showing the mean (black lines) and the distribution (colored dots) of the SMI (two-way ANOVA: $f_{(1, 4, 14583)}$ = 48.4, 210.4, and 21.3 - p < 0.001 for the region, sound level, and interaction, respectively, Fisher post hoc test, p = $6.2x10^{-4}$, $4.2x10^{-5}$, <0.001, and < 0.001 for LC vs. DC at 40, 60, 70, and 80 dB respectively) and TMI (two way ANOVA: $f_{(1, 4, 16139)}$ = 431.4, 59.1, and 8.3 - p < 0.001 for the region, sound level, and interaction, respectively, Fisher post hoc test, p = 0.002, <0.001, < 0.001, <0.001, and <0.001 for LC vs. DC at 40, 50, 60, 70, and 80 dB, respectively), respectively, across different sound levels in LC imaged via microprism (blue) vs. DC imaged directly from the dorsal surface (red) (*p<0.05, LC vs. DC). LC: Lateral cortex, DC: Dorsal cortex.

1086 **Figure 6:**

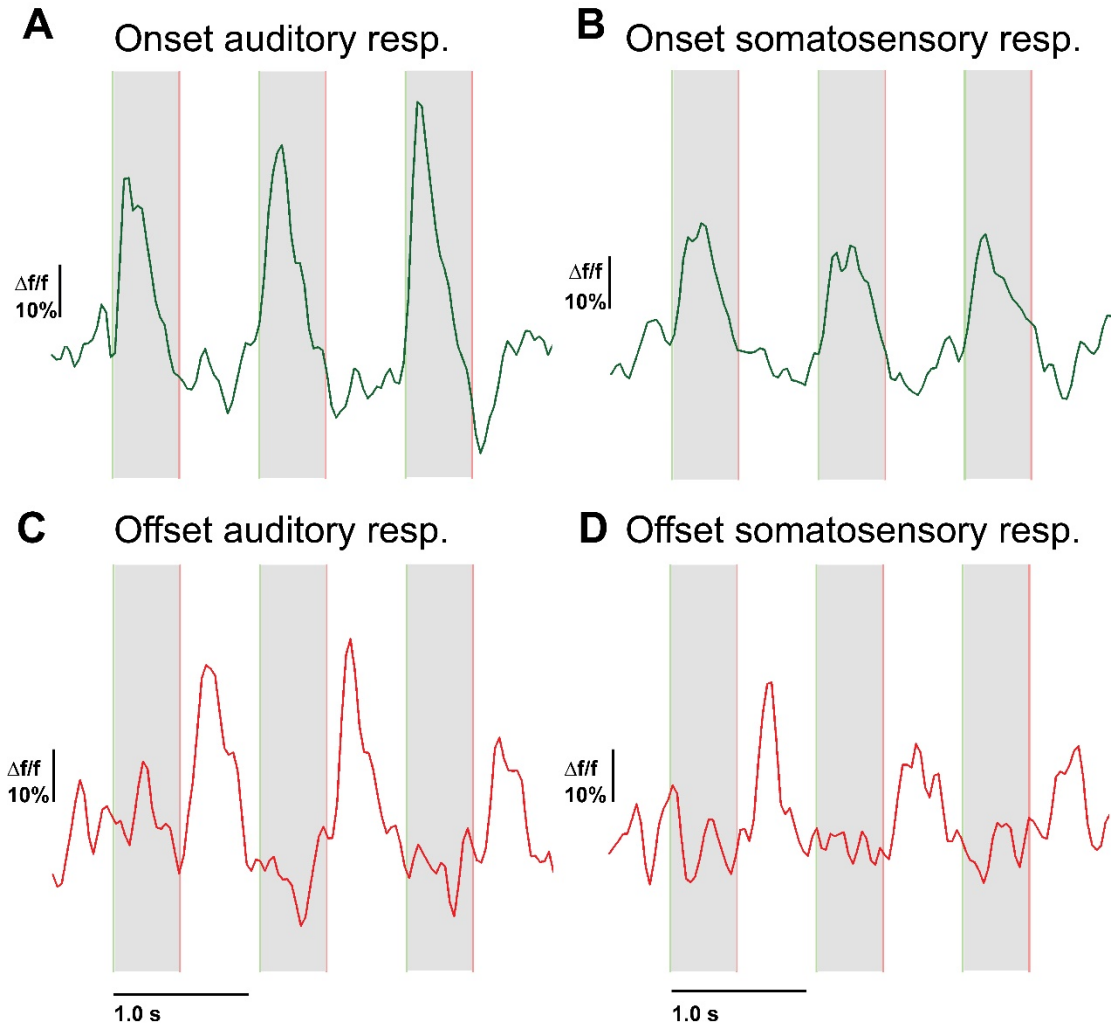

1087

1088 **Figure 6: The waveforms of the somatosensory vs. acoustic responses of the LC imaged**

1089 **via microprism.**

1090 (A-B) The time traces of the evoked calcium signals by the beginning of auditory or

1091 somatosensory stimuli, respectively (onset responses). (C-D) The time traces of the evoked

1092 calcium signals by the termination of auditory or somatosensory stimuli, respectively (offset

1093 responses).

1094

1095 **Figure 7:**

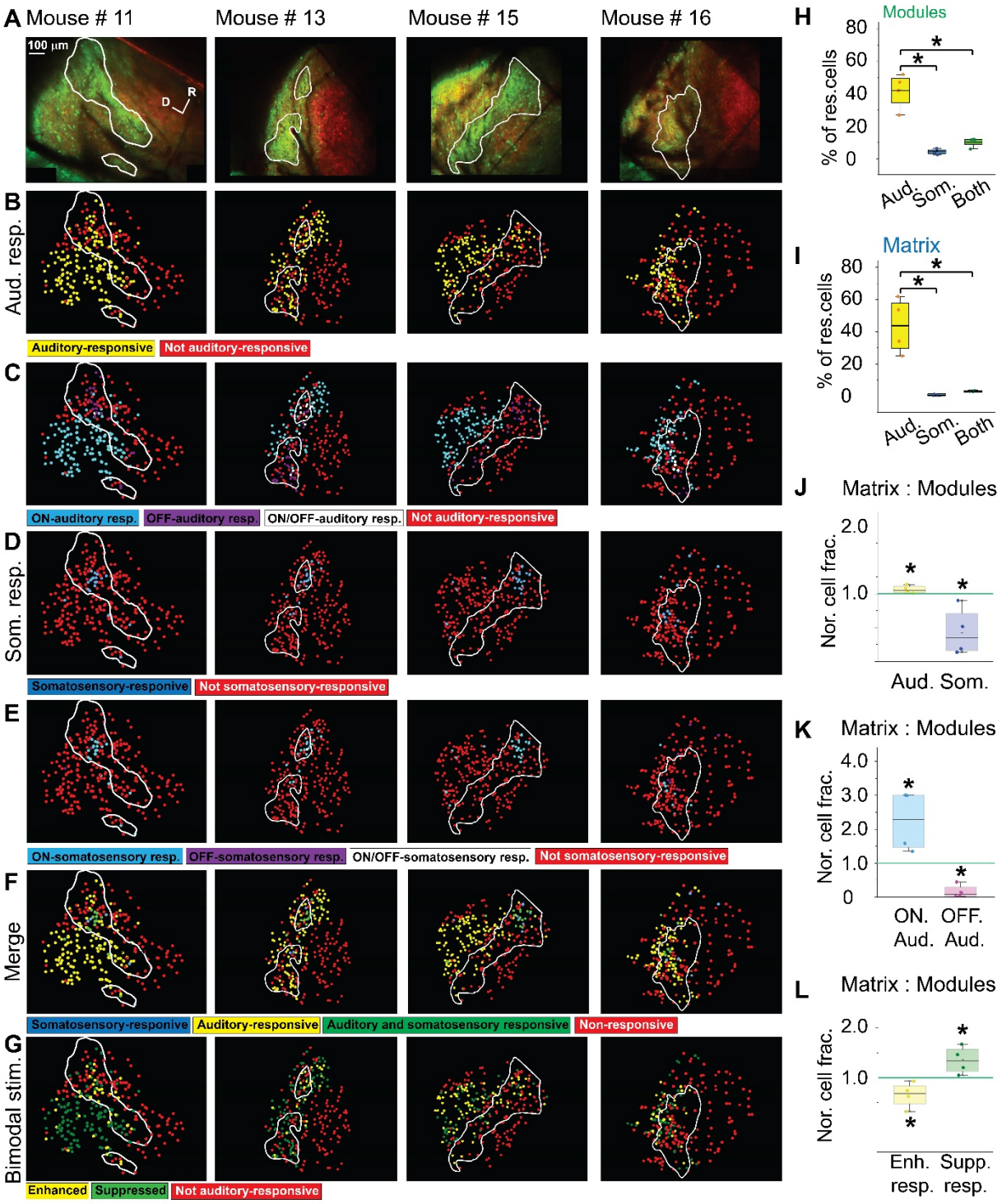

1096

1097 **Figure 7: Types of somatosensory and auditory responses from the LC neurons imaged**

1098 **via microprism.**

1099 (A) The 2P images of GFP (green) and jRGECO1a expression (red) in the LC imaged via
1100 microprism showing the modules within white irregular lines. (B, D, and F) The pseudocolor
1101 images show the auditory or somatosensory responsive cells of the LC imaged via microprism
1102 as well as the merged response, respectively (C and E) The pseudocolor images show onset
1103 (ON), offset (OFF), or onset/offset (ON/OFF) responsive cells of the LC imaged via microprism
1104 to auditory and somatosensory stimuli, respectively. (G) The pseudocolor images show
1105 enhanced and suppressive response of the auditory responsive cells of the LC imaged via
1106 microprism following the bimodal stimulation based on their response index (RI). (H and I) Bar
1107 graphs showing the percentage of responsive cells to auditory (Aud.), somatosensory (Som.),
1108 or both stimuli in modules and matrix imaged via microprism, respectively – Modules: one-way
1109 ANOVA: $f_{(2, 11)} = 38.1$ - $p = 4.0x10^{-5}$, Fisher posthoc test, $p = 1.9x10^{-5}$ or $7.6x10^{-5}$ for the
1110 percentage of responsive cells to sound only vs. the percentage of responsive cells to
1111 somatosensory stimulation only or to both, respectively and $p = 0.23$ for the percentage of
1112 responsive cells to somatosensory stimulation only vs. both, Matrix: one-way ANOVA: $f_{(2, 11)} =$
1113 23.9 - $p = 2.4x10^{-4}$, Fisher posthoc test, $p = 1.7x10^{-4}$ or $2.4x10^{-4}$ for the percentage of responsive
1114 cells to sound only vs. the percentage of responsive cells to somatosensory stimulation only or
1115 to both, respectively - $p = 0.77$ for the percentage of responsive cells to somatosensory
1116 stimulation only vs. both) (*$p<0.05$, vs. Aud.). (J) A box plot showing the normalized cell fraction
1117 of auditory (Aud.) (matrix median = 1.05) or somatosensory (Som.) (matrix median = 0.14)
1118 responsive cells in the matrix normalized to those in modules imaged via microprism (*$p<0.05$,
1119 matrix vs. modules). (K) A box plot showing the cell fraction of onset (ON. Aud.) (matrix median
1120 = 2.2) or offset (OFF. Aud.) auditory (matrix median = 0.08) responsive cells in the matrix
1121 normalized to those in modules imaged via microprism (*$p<0.05$, matrix vs. modules). (L) A box
1122 plot showing the cell fraction of the responsive cells of enhanced (Enh. resp.) or suppressive
1123 (Supp. resp.) response in the matrix normalized to those in modules imaged via microprism
1124 following bimodal stimulation (*$p<0.05$, matrix vs. modules). D: Dorsal, R: Rostral.

1125

1126

1127

1128

1129

1130

1131

1132

1133

1134

1135

1136

1137

1138

1139

1140

1141

1142 **Figure 8:**

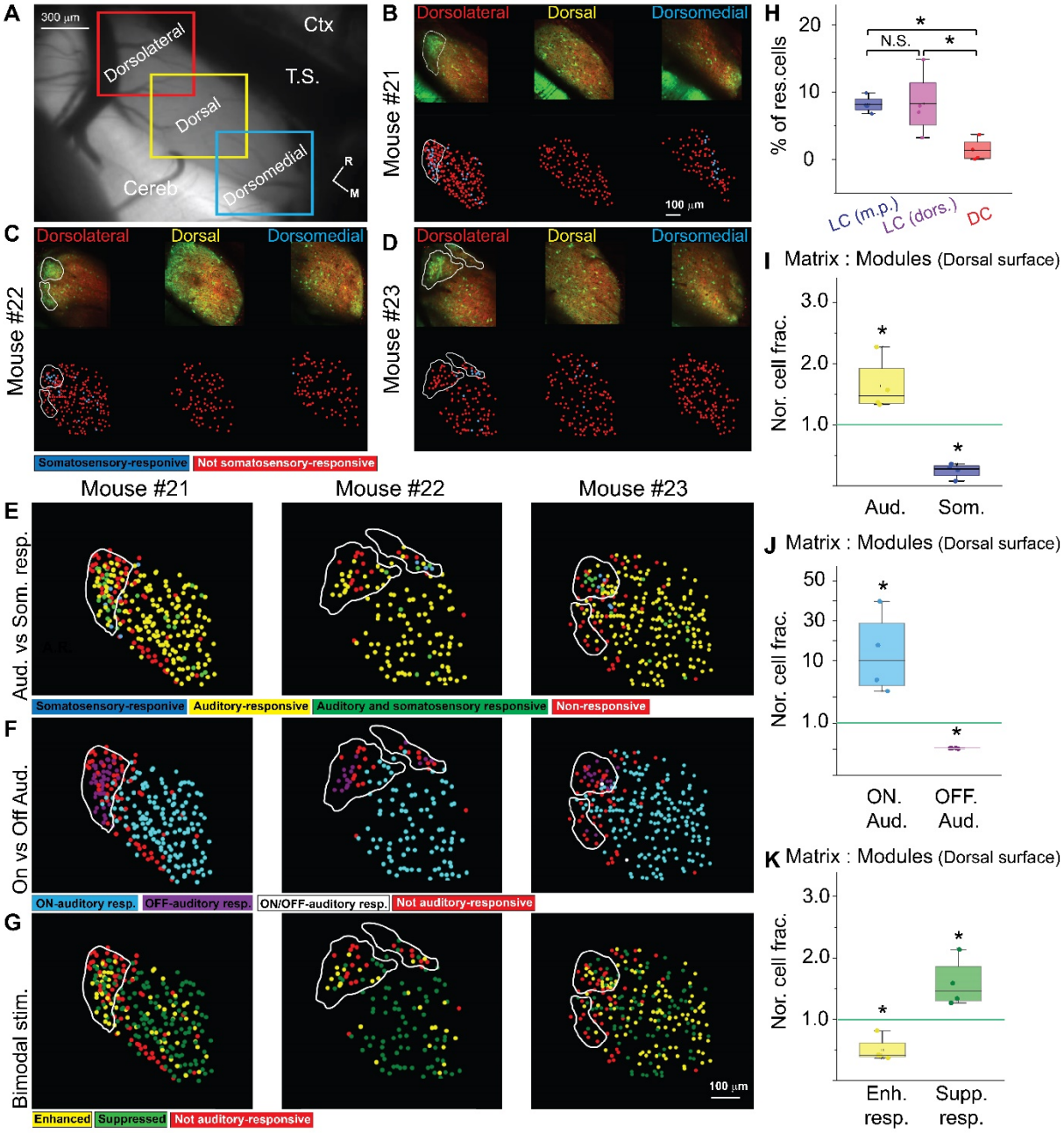

Figure 8: The somatosensory vs. auditory responses over the DC neurons.

(A) A low magnification of the image obtained from the IC surface. (B-D) The top row: The 2P images of GFP (green) and jRGECO1a expression (red) of three main regions (dorsolateral, dorsal, and dorsomedial) of the DC surface imaged from the dorsal surface showing the modules within irregular white lines in the dorsolateral region, the bottom row: The pseudocolor

1149 images show the somatosensory responsive cells after somatosensory stimulations. (E) The
1150 pseudocolor images show the responsive cells of the LC imaged from the dorsal surface to
1151 auditory and somatosensory stimulations. (F) The pseudocolor images show onset (ON), offset
1152 (OFF), or onset/offset (ON/OFF) responsive cells of the LC imaged from the dorsal surface to
1153 auditory stimulation. (G) The pseudocolor images show the enhanced and suppressive
1154 response of the auditory responsive cells of the LC imaged from the dorsal surface following the
1155 bimodal stimulation based on their response index (RI). (H) A box plot shows the percentage of
1156 somatosensory responsive cells in LC imaged either from the dorsal surface (LC (dors.)) or via
1157 microprism (LC (m. p.)) as well as the DC - one-way ANOVA: $f_{(2, 11)} = 6.7$ & $p = 0.02$, Fisher
1158 posthoc test, $p = 0.01$ or 0.01 for the percentage of somatosensory responsive cells on the DC
1159 vs. LC imaged by microprism or LC imaged from the dorsal surface, respectively - $p = 0.95$ for
1160 the percentage of somatosensory responsive cells on LC imaged via microprism vs. LC imaged
1161 from the dorsal surface) (*$p<0.05$, vs. DC). (I) A box plot showing the cell fraction of auditory
1162 (Aud.) or somatosensory (Som.) responsive cells in the matrix normalized to those in modules
1163 imaged from the dorsal surface (*$p<0.05$, matrix vs. modules). (J) A box plot showing the cell
1164 fraction of onset (ON. Aud.) or offset (OFF. Aud.) auditory responsive cells in the matrix
1165 normalized to those in modules imaged from the dorsal surface (*$p<0.05$, matrix vs. modules).
1166 (K) A box plot showing the cell fraction of the responsive cells of enhanced (Enh. Resp.) or
1167 suppressed (Supp. Resp.) responses in the matrix normalized to those in modules imaged from
1168 the dorsal surface following bimodal stimulation (*$p<0.05$, matrix vs. modules). Cereb:
1169 Cerebellum, Ctx: Cerebral cortex, M: medial, R: Rostral, TS: Transverse sinus.

1170

1171

1172

1173 **Figure 9:**

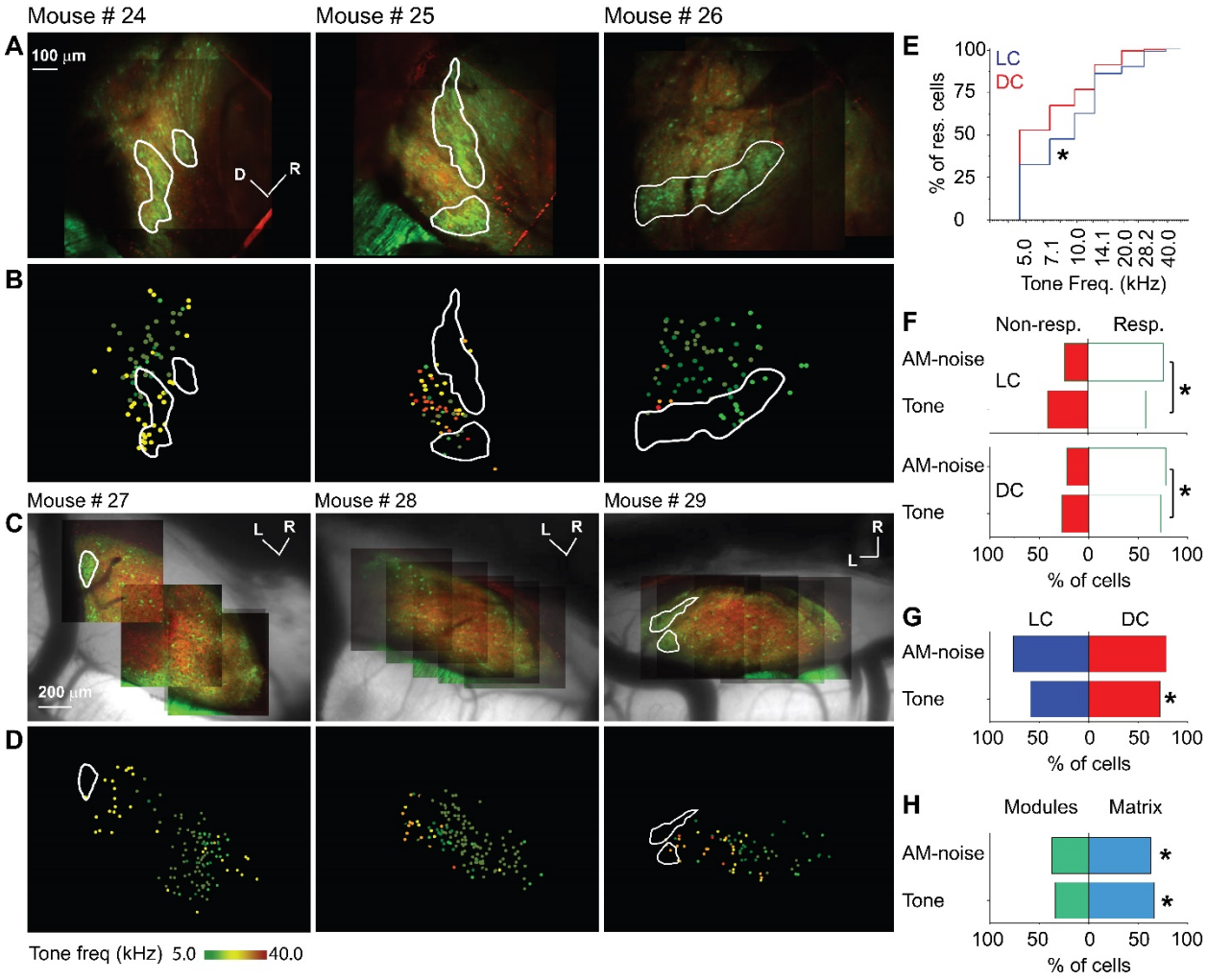

1174

1175 **Figure 9: The acoustic response from LC imaged via microprism and DC imaged from the**

1176 **dorsal surface in awake animals.**

1177 (A and C) The 2P images of GFP (green) and jRGECO1a expression (red) on either the LC

1178 surface imaged via the microprism or the DC imaged directly from the dorsal surface,

1179 respectively showing the modules within irregular white lines. (B and D) The pseudocolor

1180 images show the responsive cells to the pure tone of different combinations of frequencies and

1181 levels of the LC imaged via the microprism or the DC imaged directly from the dorsal surface,

1182 respectively. (E) The cumulative distribution function of the best tone frequencies of all cells

1183 collected either from the LC imaged via microprism (blue) or the DC (red). (F) A bar graph
1184 showing the percentage of responsive vs. nonresponsive cells to pure tone or AM-noise within
1185 the LC imaged via microprism or the DC (*$p<0.05$, pure tone vs. AM-noise). (G) A bar graph
1186 showing the percentage of responsive cells to pure tone or AM-noise for LC imaged via
1187 microprism vs. DC (*$p<0.05$, LC vs. DC). (H) A bar graph showing the percentage of responsive
1188 cells to pure tone or AM-noise for modules vs. matrix imaged via microprism(*$p<0.05$, matrix vs.
1189 modules). D: Dorsal, L: Lateral, Non-resp.: Non-responsive, Resp.: Responsive, R: Rostral.

1190

1191

1192

1193

1194

1195

1196

1197

1198

1199

1200

1201

1202

1203

Figure 10:

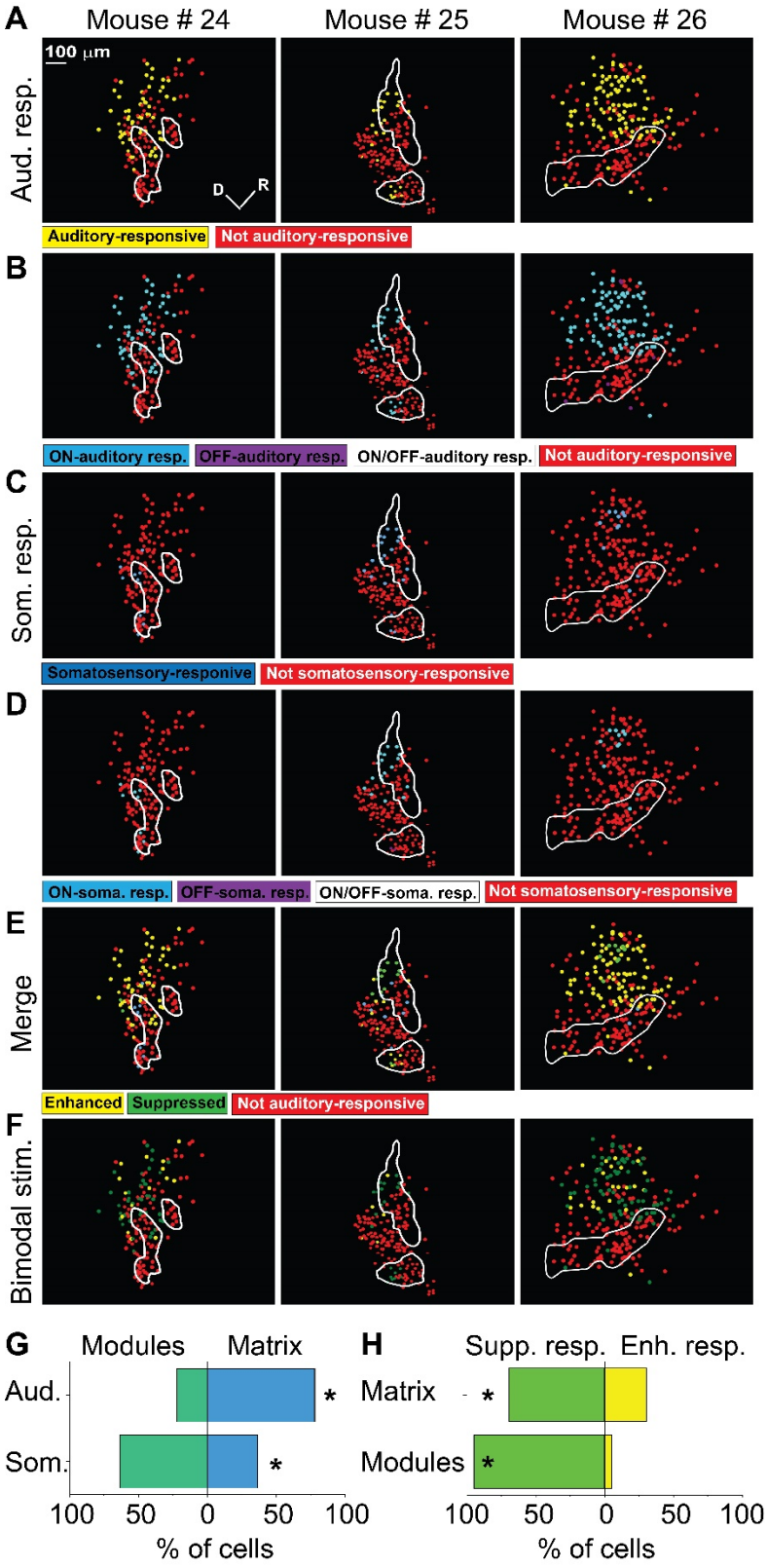
A
Mouse # 24
Mouse # 25
Mouse # 26
Aud. resp.
100 μm
D
R
Auditory-responsive
Not auditory-responsive
B
ON-auditory resp.
OFF-auditory resp.
ON/OFF-auditory resp.
Not auditory-responsive
C
Som. resp.
Somatosensory-responive
Not somatosensory-responsive
D
ON-soma. resp.
OFF-soma. resp.
ON/OFF-soma. resp.
Not somatosensory-responsive
E
Merge
Enhanced
Suppressed
Not auditory-responsive
F
Bimodal stim.
G
Modules
Matrix
Aud.
Som.
*
*
100
50
0
50
100
% of cells
H
Supp. resp.
Enh. resp.
Matrix
Modules
*
*
100
50
0
50
100
% of cells

1206 **Figure 10: The somatosensory response from LC imaged via microprism in awake**
1207 **animals.**

1208 (A, C, and E) The pseudocolor images show the auditory or somatosensory responsive cells of
1209 the LC imaged via microprism to auditory and somatosensory stimulations as well as the
1210 merged response, respectively. (B and D) The pseudocolor images show onset (ON), offset
1211 (OFF), or onset/offset (ON/OFF) responsive cells of the LC imaged via microprism to auditory
1212 and somatosensory stimulations, respectively. (F) The pseudocolor images show the enhanced
1213 or suppressed responses of the auditory responsive cells following the bimodal stimulation
1214 based on their response index (RI). (G) A bar graph showing the cell fraction of auditory (Aud.)
1215 or somatosensory (Som.) responsive cells in the matrix vs. modules imaged via microprism
1216 (*$p<0.05$, matrix vs. modules). (H) A bar graph showing the cell fraction of the responsive cells
1217 of suppressed (Supp. resp.) or enhanced (Enh. resp.) response in the matrix vs. modules
1218 imaged via microprism following bimodal stimulation (*$p<0.05$, low vs. high response). D:
1219 Dorsal, R: Rostral.

1220